

**LATTICE BOLTZMANN  
SIMULATION OF IMMISCIBLE  
TWO PHASE FLOW AT THE PORE  
SCALE**

**A REPORT SUBMITTED TO THE DEPARTMENT OF ENERGY  
RESOURCES ENGINEERING**

**OF STANFORD UNIVERSITY**

**IN PARTIAL FULFILLMENT OF THE REQUIREMENTS FOR THE  
DEGREE OF MASTER OF SCIENCE**

**By  
Wenshi Chen  
January 2011**



I certify that I have read this report and that in my opinion it is fully adequate, in scope and in quality, as partial fulfillment of the degree of Master of Science in Energy Resources Engineering.

---

Prof. Hamdi Tchelepi



# Abstract

Modeling multiphase flow at the pore scale is of interest to better understand and predict the complex flow dynamics in large-scale natural porous media. Based on the Lattice Boltzmann Method (LBM), we simulated the flow of two immiscible fluids in 2D and 3D pore spaces. LBM simulations seem to capture the essential physics associated with imbibition and drainage processes at the pore scale. In order to model the evolution of immiscible two-phase flow in the presence of viscosity and density differences, a great deal of effort is still needed, including physically motivated models of solid-fluid contact lines and accurate resolution of fluid-fluid interfaces.



## Acknowledgments

This work was sponsored by the Stanford Industrial Consortium on Reservoir Simulation (SUPRI-B) and advised by Prof. H. Tchelepi. Especially, I appreciate the technical support by R. Clapp from CEES, Stanford University and Dr. Q. Kang from the Los Alamos National Laboratory, who provided me with an LBM simulator, which served as a basis for this work.

.





# Contents

Abstract .....	v
Acknowledgments.....	vii
Contents .....	ix
List of Tables .....	xi
List of Figures .....	xiii
1. Introduction.....	1
1.1. LBM as an DNS Technique.....	1
1.1.1. LBM for Single Phase Flow .....	1
1.1.2. MultiRelaxation-Time LBM.....	4
1.2. Multiphase Simulation with LBM .....	5
1.2.1. Color-Fluid Model .....	6
1.2.2. Shan-Chen's Model .....	6
1.2.3. Free-Energy Model .....	9
1.2.4. Mean-Field Model .....	11
1.3. Numerical Boundary Condition.....	12
1.3.1. Fluid Boundary Condition .....	12
1.3.2. Solid Boundary Condition .....	14
1.4. Parallel Computing .....	14

2. Results.....	17
2.1. Hele-Shaw Flow.....	17
2.1.1. Effect of $M$ .....	19
2.1.2. Effect of $g_w$ .....	21
2.1.3. Effect of $m^2$ .....	22
2.1.3. Comparison with Theoretical Solution .....	22
2.2. Single Phase Flow in Three Dimensions .....	23
2.3. Simulating CO <sub>2</sub> -Water Flow in Sandstone .....	27
2.3.1. Model Description .....	27
2.3.2. Parameter Calibration .....	28
2.3.3. Steady State Distribution in Porous Media.....	33
2.3.4. Water Drainage and Imbibition .....	33
3. Conclusions.....	45
References.....	47

## List of Tables

Table 1 Parameter Option for Simulation.....	17
Table 2 Simulated and Theoretical Finger Widths .....	21
Table 3 Dimensionless Parameters in Single Phase Simulation.....	24
Table 4 Physical Properties of Water and CO <sub>2</sub> .....	27



# List of Figures

Figure 1 Schematic Illustration of Fingering Chanel.....	15
Figure 2 Interface Evolutions for $M = 1$ : (a) Simulation 1, (b) Simulation 2, and (c) Simulation 3 .....	18
Figure 3 Interface Evolutions for $M = 4$ : (a) Simulation 4, (b) Simulation 5, and (c) Simulation 6 .....	18
Figure 4 Interface Evolutions for $M = 10$ : (a) Simulation 7, (b) Simulation 8, and (c) Simulation 9 .....	19
Figure 5 Interface Evolutions with $g_{1w} = -0.03, 0$ and $0.03$ : (a) Simulation 10, (b) Simulation 3, and (c) Simulation 11 .....	20
Figure 6(a)-(c) Interface Evolutions with $m^2 = 0.6, 1$ and $1.4$ : (a) Simulation 12, (b) Simulation 3, and (c) Simulation 13 .....	21
Figure 7 Glass Bead Pack: Blue for the Glass Beads .....	23
Figure 8 Relation between Dimensionless Parameters:.....	25
Figure 9 Pore Structure of the Sandstone: Yellow for Void and White for Rock .....	26
Figure 10 Pressure-Density Curve: (a) CO <sub>2</sub> , (b) Water .....	29
Figure 11 Modified Pore Structure of Sandstone: Yellow for Void and White for Rock .....	33
Figure 12 Phase Distribution in Pore Space: Red for CO <sub>2</sub> , Yellow for Water and White for Rock: (a)-(c) $S_{CO_2} = 0.42$ , $t = 0, 500$ and $1000 \Delta t$ ;(a)-(c) $S_{CO_2} = 0.6221$ , $t = 0, 500$ and $1000 \Delta t$ .....	36
Figure 13 Snapshots of CO <sub>2</sub> Plume in Fontainebleau Sandstone during Water Drainage, from $t = 0$ to $t = 20000\Delta t$ with interval of $5000\Delta t$ : Red for CO <sub>2</sub> , Yellow for Water and White for Sandstone Grains .....	43
Figure 14 Snapshots of CO <sub>2</sub> Plume in Fontainebleau Sandstone at the End of Water Imbibition.....	44



# Chapter 1

## 1. Introduction

Many energy resource recovery and environmental remediation processes involve multiphase flow in natural porous media, such as Enhanced Oil Recovery (EOR) and CO<sub>2</sub> sequestration in deep aquifers. Direct Numerical Simulation (DNS) of multiphase flow is needed to describe the details of the physics that governs multiphase flow and transport in porous media, which can serve as a strong basis to model the behavior at the so-called Darcy and larger scales.

To perform DNS, one needs: (1) knowledge of the pore space geometry, (2) specification of the initial distribution of the fluids and the boundary conditions at all the solid-fluid and fluid-fluid boundaries, and (3) accurate solution of the governing equations. The development of Micro X-ray Computed Tomography (MicroCT) techniques has managed to fulfill the first condition. The second requirement poses the most significant challenge at this time. The third item must meet several criteria: First, the numerical method must model the fluid flow consistently with the governing physical principals. Second, the numerical method should be suitable for a wide range of simulation settings to tackle the different type of porous media and flow conditions. In addition, the computational cost of the numerical method must not be prohibitively high. We employ the Lattice Boltzmann Method (LBM) as the numerical simulation framework in our work.

### 1.1. Lattice Boltzmann Method (LBM)

The Lattice Boltzmann Method (LBM) is a numerical scheme for simulating fluid flow (Chen, S. and Doolen G., 1998). The basic idea of LBM is to simulate simplified kinetic models of microscopic processes, so that the macroscopic equations can be obeyed by the macroscopic averaged properties (Chen, S. and Doolen G., 1998). First proposed in the 1980's (Frisch, U. *et al.*, 1986) (Frisch, U. *et al.*, 1987), LBM has become a promising numerical method for modeling complex fluid flow phenomena (Chen, S. and Doolen G., 1998).

#### 1.1.1. A Simple LBM for the Ideal Gas Model

LBM originated from the Lattice Gas Automata (LGA) approach (Frisch, U. *et al.*, 1986). The approach is based on the Boltzmann Equation, written as (Bhatnagar, P. *et al.*, 1954)

$$\frac{\partial f}{\partial t} + \mathbf{v} \cdot \frac{\partial f}{\partial \mathbf{x}} + \mathbf{F} \cdot \frac{\partial f}{\partial \mathbf{v}} = \left. \frac{\partial f}{\partial t} \right|_{\text{collision}} \quad \text{Eq. 1}$$

where  $\mathbf{v}$  is the velocity of a molecule,  $\mathbf{F}$  is the external force,  $f(\mathbf{v}, \mathbf{x})$  is the distribution function of molecules with velocity and position  $(\mathbf{v}, \mathbf{x})$ , and  $\left. \frac{\partial f}{\partial t} \right|_{\text{collision}}$  is the rate of change of the distribution caused by molecular collisions.

According to Enskog's theory for ideal gases (Bhatnagar, P. *et al.*, 1954), the collision term  $\left. \frac{\partial f}{\partial t} \right|_{\text{collision}}$  can be simplified as

$$\left. \frac{\partial f}{\partial t} \right|_{\text{collision}} \approx \frac{f - f^{eq}}{\tau^*} \quad \text{Eq. 2}$$

by neglecting the size of the molecule. This treatment is referred to as Bhatnagar-Gross-Krook (BGK) model. Here,  $\tau^*$  is the relaxation time of the collision process, and  $f^{eq}$  is the equilibrium distribution function (He, X. and Doolen, G., 2002)

$$f^{eq} = \frac{\rho}{(2\pi RT)^{\frac{3}{2}}} e^{-\frac{(\mathbf{v}-\mathbf{u})^2}{2RT}} \quad \text{Eq. 3}$$

where  $\mathbf{u}$  and  $\rho$  are the macroscopic velocity and density, respectively,  $R$  is the gas constant and  $T$  is the temperature.

In order to solve Eq. 1 using a finite-difference (FD) method, the domain is discretized into a square lattice with lattice spacing,  $\Delta x$ , and time is discretized into increments,  $\Delta t$ , and the velocity space,  $\mathbf{v}$ , is also discretized into a set of discrete velocities. The velocity discretization of LBM is usually denoted in the form of “D $l$ Q $m$ ” where  $l$  denotes the dimensionality and  $m$  denotes the number of discrete velocities in the lattice model. The D2Q9 and D3Q19 LBM are widely used for two-dimensional and three-dimensional simulations. In a D2Q9 model,  $\mathbf{v}$  is usually discretized into nine velocities (Chen, S. and Doolen G., 1998):

$$\mathbf{e}_i = \begin{cases} (0,0), i=1 \\ (\pm 1,0), (0,\pm 1), i=2-5 \\ (\pm 1,\pm 1), i=6-9 \end{cases} \quad \text{Eq. 4}$$

where the unit is the lattice speed  $\frac{\Delta x}{\Delta t}$ . The distribution function  $f(\mathbf{x}, \mathbf{v}, t)$  is discretized into  $f_i = f(\mathbf{x}, \mathbf{e}_i, t)$ ,  $i=0, \dots, 8$  as well. The lattice size  $\Delta x$  must be much larger than the molecule to ensure the validity of ensemble averaging. In the D3Q19 model, the discrete velocities are chosen to be (Kang, Q. *et al.*, 2005):



$$\mathbf{e}_i = \begin{cases} (0,0,0), i=1 \\ (\pm 1, 0, 0), (0, \pm 1, 0), (0, 0, \pm 1), i=2-7 \\ (\pm 1, \pm 1, 0), (0, \pm 1, \pm 1), (\pm 1, 0, \pm 1), i=8-19 \end{cases} \quad \text{Eq. 5}$$

in units of lattice speed.

Analogous to Gaussian quadrature, the discrete molecular density  $f_i$  satisfies the relation:

$$n(\mathbf{x}, t) = \int f(\mathbf{v}, \mathbf{x}, t) d\mathbf{x} = \sum_{i=1}^m f_i(\mathbf{x}, t) \quad \text{Eq. 6}$$

$$n(\mathbf{x}, t) \mathbf{u}(\mathbf{x}, t) = \int f(\mathbf{v}, \mathbf{x}, t) d\mathbf{v} = \mathbf{u}(\mathbf{x}, t) \sum_{i=1}^m f_i(\mathbf{x}, t) \mathbf{e}_i \quad \text{Eq. 7}$$

where  $n(\mathbf{x}, t)$  is the macroscopic molar density. Neglecting the external body force and applying an explicit upwind FD method to Eq. 1, we obtain the Lattice Boltzmann Equation (LBE) (Chen, S. and Doolen G., 1998)

$$f_i(\mathbf{x} + \mathbf{e}_i \Delta t, t + \Delta t) - f_i(\mathbf{x}, t) = \frac{f_i - f_i^{eq}}{\tau}, \quad \text{Eq. 8}$$

where  $\tau = \frac{\tau^*}{\Delta t}$  is the dimensionless relaxation time, and  $f_i^{eq}$  is the equilibrium distribution of velocity  $\mathbf{e}_i$ . In the D2Q9 LBM model, the equilibrium distribution is given as (Qian, Y. *et al.*, 1992):

$$\begin{cases} f_1^{eq} = n \left( d_0 - \frac{\Delta t^2}{\Delta x^2} \mathbf{u} \cdot \mathbf{u} \right), \\ f_i^{eq} = 4n \left[ \frac{1-d_0}{20} + \frac{\Delta t^2}{12\Delta x^2} \mathbf{e}_i \cdot \mathbf{u} + \frac{\Delta t^4}{8\Delta x^4} (\mathbf{e}_i \cdot \mathbf{u})^2 - \frac{\Delta t^2}{24\Delta x^2} \mathbf{u} \cdot \mathbf{u} \right], i=2-5 \\ f_i^{eq} = n \left[ \frac{1-d_0}{20} + \frac{\Delta t^2}{12\Delta x^2} \mathbf{e}_i \cdot \mathbf{u} + \frac{\Delta t^4}{8\Delta x^4} (\mathbf{e}_i \cdot \mathbf{u})^2 - \frac{\Delta t^2}{24\Delta x^2} \mathbf{u} \cdot \mathbf{u} \right], i=6-9 \end{cases} \quad \text{Eq. 9}$$

In the D3Q19 LBM model, the equilibrium distribution is given as:

$$\begin{cases} f_1^{eq} = n \left( d_0 - \frac{\Delta t^2}{2\Delta x^2} \mathbf{u} \cdot \mathbf{u} \right), \\ f_i^{eq} = 2n \left[ \frac{1-d_0}{24} + \frac{\Delta t^2}{12\Delta x^2} \mathbf{e}_i \cdot \mathbf{u} + \frac{\Delta t^4}{8\Delta x^4} (\mathbf{e}_i \cdot \mathbf{u})^2 - \frac{\Delta t^2}{24\Delta x^2} \mathbf{u} \cdot \mathbf{u} \right], i = 2-7 \\ f_i^{eq} = n \left[ \frac{1-d_0}{24} + \frac{\Delta t^2}{12\Delta x^2} \mathbf{e}_i \cdot \mathbf{u} + \frac{\Delta t^4}{8\Delta x^4} (\mathbf{e}_i \cdot \mathbf{u})^2 - \frac{\Delta t^2}{24\Delta x^2} \mathbf{u} \cdot \mathbf{u} \right], i = 8-19 \end{cases} \quad \text{Eq. 10}$$

Here  $d_0$  is the fraction of stationary molecules at equilibrium and  $w_i$  is the corresponding distribution at  $\mathbf{u} = \mathbf{0}$ . Since they are obtained using Taylor expansions, these equilibrium distributions are valid only when  $|\mathbf{u}| \ll \frac{\Delta x}{\Delta t}$ .

From the Chapman-Enskog expansion, one can recover the incompressible Navier-Stokes equations at low frequency and in the long wavelength limit (Chen, S. and Doolen G., 1998). This suggests that simulation results of the above-mentioned LBM are valid only when  $|\mathbf{u}| \ll c_s$ , which is the speed of sound in the fluid, and  $\frac{Dn(\mathbf{x}, t)}{Dt} \ll 1$ ,

where  $\frac{D}{Dt}$  is the temporal material derivative.

In implementing LBM, updating the molecular distribution can be accomplished in two steps. The value of  $f_i(\mathbf{x}, t)$  is first updated to  $f_i(\mathbf{x} + \mathbf{e}_i \Delta t, t + \Delta t)$ , which is called the streaming step, and then the value of  $f_i(\mathbf{x} + \mathbf{e}_i \Delta t, t + \Delta t)$  is changed by  $\frac{f_i - f_i^{eq}}{\tau}$ , which is called the collision step. The LBM equation for 3D models can be defined likewise. Using the Chapman-Enskog expansion, one can derive the Navier-Stokes equations and Euler equations from the LBM equations for incompressible flow (Chen, H. *et al.*, 1992). In other words, the LBM equations can easily model incompressible single-phase flow.

### 1.1.2. MultiRelaxation-Time LBM

It is well known that the stability of an explicit scheme for Partial Differential Equations (PDE) is conditional. Although theoretically one can derive implicit LBM equations that are unconditionally stable, the extremely large size of the linear system will render the idea impractical. Also, the LBM equation with the BGK collision operator suffers from a fixed Prandtl number and a fixed ratio between the kinematic viscosity and dynamic viscosity (d'Humières, D., 2002). In order to overcome these deficiencies, d'Humières proposed the so-called MultiRelaxation-Time (MRT) LBM scheme (d'Humières, D., 1992).

We describe the scheme for a D2Q9 LBM model. In the BGK model, the collision operator is applied on the linear space  $V$  spanned by  $\mathbf{e}_0, \dots, \mathbf{e}_8$ . In the MRT model, however, a set of linearly independent moments of  $f_i$  is chosen to construct a new linear space  $W$ . Specifically, these moments are chosen and expressed with the coordinates  $(\mathbf{e}_0, \dots, \mathbf{e}_8)$  (Lallemand, P. and Luo, L., 2000):

$$\left\{ \begin{array}{l} \rho = (1, 1, 1, 1, 1, 1, 1, 1, 1)^T \\ e = (-4, -1, -1, -1, -1, 2, 2, 2, 2)^T \\ \varepsilon = (4, 2, 2, 2, 2, 1, 1, 1, 1)^T \\ j_x = (0, 1, 0, -1, 0, 1, -1, -1, 1)^T \\ q_x = (0, -2, 0, 2, 0, 1, -1, -1, 1)^T \\ j_y = (0, 0, 1, 0, -1, 1, 1, -1, -1)^T \\ q_y = (0, 0, -2, 0, 2, 1, 1, -1, -1)^T \\ p_{xx} = (0, 1, -1, 1, -1, 0, 0, 0, 0)^T \\ p_{xy} = (0, 0, 0, 0, 0, 1, -1, 1, -1)^T \end{array} \right. \quad \text{Eq. 11}$$

These moments are linearly independent and orthogonal. Therefore, they span a linear space denoted as  $W$  with clear physical meanings (Lallemand, P. and Luo, L., 2000). Denote  $\mathbf{M}$  as the transition matrix from  $V$  to  $W$  and  $\mathbf{f} = (f_0, \dots, f_8)$  as a vector in  $V$  with  $\mathbf{m} = \mathbf{M} \cdot \mathbf{f}$  as the vector corresponding to  $\mathbf{f}$  in  $W$ . Similar to the BGK model, the LBM equation of the MRT model is written as (d'Humières, D., 2002):

$$\left( f_i(\mathbf{x} + \mathbf{e}_i \Delta t, t + \Delta t) \right)_{i=0, \dots, 9} - \mathbf{f}(\mathbf{x}, t) = -\mathbf{M}^{-1} \hat{\mathbf{S}} (\mathbf{m}(\mathbf{x}, t) - \mathbf{m}^{eq}(\mathbf{x}, t)) \quad \text{Eq. 12}$$

where  $\hat{\mathbf{S}} = \text{diag}(s_0, \dots, s_8)$  with  $s_i^{-1}$  as the relaxation time of each component in  $W$  and  $\mathbf{m}^{eq}(\mathbf{x}, t)$  is the local equilibrium of  $\mathbf{m}(\mathbf{x}, t)$ . Some of the moments defined in Eq. 11 are conserved during collision, such as the density  $\rho$  and momentum  $j$  (d'Humières, D., 2002). Therefore, the corresponding coefficient  $s_i$  should be set to zero.

Denoting  $\mathbf{S} = \mathbf{M}^{-1} \cdot \hat{\mathbf{S}} \cdot \mathbf{M}$ , Eq. 8 can be simplified as (d'Humières, D., 2002):

$$\left( f_i(\mathbf{x} + \mathbf{e}_i \Delta t, t + \Delta t) \right)_{i=0, \dots, 9} - \mathbf{f}(\mathbf{x}, t) = -\mathbf{S} (\mathbf{f}(\mathbf{x}, t) - \mathbf{f}^{eq}(\mathbf{x}, t)). \quad \text{Eq. 13}$$

Although the MRT-LBM has several advantages over BGK-LBM, we chose the BGK-LBM approach in this study because we are interested in understanding the basics of LBM simulations for immiscible two-phase flow in porous media.

## 1.2. Multiphase Simulation with LBM

Numerical simulation of multiphase fluid flow is a challenging problem due to the difficulty in modeling interface dynamics (Chen, S. and Doolen, G., 1998). Since the 1990s, several models have been proposed to simulate multiphase fluid flow with LBM (Gunstensen *et al.*, 1991) (Shan, X. and Chen, H., 1993) (Swift, M. *et al.*, 1995) (He, X *et al.*, 1999). There are several reported advantages of LBM over traditional numerical methods in modeling multiphase flow, like the flexibility to capture the interfacial dynamics and complex boundaries (Kang, Q. *et al.*, 2002). There are, however, many open questions about the basic models of solid-fluid and fluid-fluid interfaces in porous media. In this section, we will review some typical multiphase models based on LBM.

### 1.2.1. Color-Fluid Model

The color-fluid model was first proposed by Gunstensen in 1991 and then improved by Grunau *et al.* in 1993. In this model, the two phases under study are labeled “blue” (b) and “red” (r), respectively. The RHS of Eq. (7), known as the collision operator  $\Omega_i^{*k} = (\Omega_i^k)_1 + (\Omega_i^k)_2$  has two terms. The first

term  $(\Omega_i^k)_1 = -\frac{\Delta x}{\tau^k} (f_i^k(\mathbf{x}, t) - f_i^{k(eq)}(\mathbf{x}, t))$  is the same as the operator defined in the BGK model with  $\tau^k$  as the relaxation time of the  $k$ th component. The second term is a perturbation on the first one, and is written as:

$$(\Omega_i^k)_2 = \frac{A^k}{2} \|\mathbf{P}\| \left( \frac{(\mathbf{e}_i \cdot \mathbf{P})^2}{\|\mathbf{P}\|^2} - \frac{1}{2} \right) \quad \text{Eq. 14,}$$

where  $\mathbf{P}$  is the local color gradient defined by:

$$\mathbf{P}(\mathbf{x}) = \sum_i \mathbf{e}_i (n^r(\mathbf{x} + \mathbf{e}_i \Delta t) - n^b(\mathbf{x} + \mathbf{e}_i \Delta t)) \quad \text{Eq. 15}$$

and  $A^k$  is the parameter controlling the interface strength. Obviously, the effect of the second term is to redistribute the molecules according to the color gradient.

Although intuitive, the color-fluid model is purely phenomenological and may suffer from relatively poor computational efficiency (Hou *et al.*, 1997). It is reported that the color-fluid model does not reproduce the bubble test in accordance with Laplace’s law. Also the maximum surface tension allowed for color-fluid is smaller than the Shan-Chen’s model.

### 1.2.2. Shan-Chen’s Model

Compared with the simple LBM approach for ideal gas, the Shan-Chen's model incorporates interactions with nearest neighbors in space (Shan, X. and Chen, H., 1993). The equilibrium macroscopic velocity should satisfy:

$$\rho^k \mathbf{u}^{k(eq)} = \rho^k \mathbf{u}' + \tau^k \mathbf{F}^k \quad \text{Eq. 16}$$

Where  $\mathbf{u}'$  is weighted average of  $\mathbf{u}^k$  and  $\mathbf{F}^k = \mathbf{F}_1^k + \mathbf{F}_2^k + \mathbf{F}_3^k$  is the total non-contacting force on the  $k$ th component. Combining Eq. 8, Eq. 9 and Eq. 16, the LBE for each component can be obtained.

The three components of  $\mathbf{F}^k$  are fluid-fluid interaction,  $\mathbf{F}_1^k$ , fluid-solid interaction,  $\mathbf{F}_2^k$ , and the external body force,  $\mathbf{F}_3^k$ . Eq. 16 can be rewritten as

$$\frac{\rho^k}{\tau^k} \mathbf{u}^{k(eq)} = \frac{\rho^k}{\tau^k} \mathbf{u}' + \mathbf{F}^k. \quad \text{Eq. 17}$$

This equation must hold in the absence of external forces, i.e.  $\mathbf{F}^k = 0$ , to guarantee the conservation of momentum. Summing up both sides of Eq. 16 over all the components, the value of  $\mathbf{u}'$  is found as

$$\mathbf{u}' = \frac{\sum_{k=1}^s \frac{\rho^k}{\tau^k} \mathbf{u}^k}{\sum_{k=1}^s \frac{\rho^k}{\tau^k}}. \quad \text{Eq. 18}$$

The interactive force between the  $k$ th component and the  $k'$ th component located at  $\mathbf{x}$  and  $\mathbf{x}'$  is defined as (Shan, X. and Chen, H., 1993):

$$\mathbf{F}_1^k = -\psi_k(\mathbf{x}) \sum_{\mathbf{x}'} \sum_{k=1}^s G_{kk'}(\mathbf{x}, \mathbf{x}') \psi_{k'}(\mathbf{x}') (\mathbf{x}' - \mathbf{x}), \quad \text{Eq. 19}$$

where the “effective mass”  $\psi_k(\mathbf{x}) = \Psi(n^k(\mathbf{x}))$  is a function depending on the local density and  $G_{kk'}(\mathbf{x}, \mathbf{x}')$ , which is the Green function of the potential between components. In this study, only interactions between adjacent lattice points are considered, i.e.,

$$G_{kk'}(\mathbf{x}, \mathbf{x}') = \begin{cases} g_{kk'}, & |\mathbf{x} - \mathbf{x}'| = \Delta x \\ \varepsilon g_{kk'}, & |\mathbf{x} - \mathbf{x}'| = \sqrt{2}\Delta x \\ 0, & \text{otherwise} \end{cases} \quad \text{Eq. 20}$$

where  $\varepsilon$  is a coefficient for increasing the isotropy of the model depending on the LBM structure (Yuan, P. and Schaefer, L., 2006). Usually,  $\varepsilon = \frac{1}{4}$  is used in the D2Q19 LBM model, and  $\varepsilon = \frac{1}{2}$  is used in the D3Q19 LBM model.

In their original work, Shan and Chen indicate that the value of  $\Psi(n)$  should be monotonically increasing with  $n$  and bounded. Subsequently,  $\Psi(n) = n_0 \left( 1 - e^{-\frac{n}{n_0}} \right)$  is chosen and proven to be effective in modeling the phase behavior of the water-steam system (Shan, X. and Chen, H., 1993). Several cubic Equations of State (EoS) are used to derive  $\Psi(n)$ , which can lead to very good agreement with theoretical predictions of the phase behavior (Yuan, P. and Schaefer, L., 2006). It has been demonstrated, however, that the only choice of  $\Psi(n)$  consistent with the thermodynamic surface tension is  $\Psi(n) = n$  (He, X. and Doolen, G., 2002). By choosing  $\Psi(n) = n$ , however, there would be no limitation on the molecular number in a lattice cell, which can lead to unbounded growth in molecule density. These conflicting trends can be reconciled by choosing  $\Psi(n) = \begin{cases} n, n \leq n_0 \\ n_0, n > n_0 \end{cases}$  (He, X. and Doolen, G., 2002). The reason is quite straightforward. Given the validity range of LBM, it must be guaranteed that the relative variation  $\frac{\Delta n(\mathbf{x})}{n(\mathbf{x})}$  is very small. As a result,  $n_0 \left( 1 - e^{-\frac{n}{n_0}} \right) \approx n$  to the first order, if  $n_0 = \langle n \rangle$ . This treatment can also prevent the instability in molecular density.

There are several other issues associated with the “effective mass” in Shan-Chen’s model. The surface tension produced by Shan-Chen’s model is actually a numerical artifact rather than a physical property (He, X. and Doolen, G., 2002). The magnitude of the tension is fixed by  $g_{kk}$ . Also, it is difficult to generate a very sharp interface using Shan-Chen’s model (He, X. and Doolen, G., 2002). To overcome these disadvantages, a modified Shan-Chen’s model called the multirange Shan-Chen’s model was proposed (Sbragaglia, M. *et al.*, 2007), which is beyond the scope of this report.

The fluid-solid interaction  $\mathbf{F}_2^k$  is defined similarly by (Shan, X. and Chen, H., 1993)

$$\mathbf{F}_2^k = -n^k(\mathbf{x}) \sum_{\mathbf{x}'} g_{k\mathbf{w}} n^w(\mathbf{x}') (\mathbf{x}' - \mathbf{x}) \quad \text{Eq. 21}$$

where  $n^w$  is the molar density of the solid defined by  $n^w(\mathbf{x}) = \begin{cases} n^w, \text{solid} \\ 0, \text{fluid} \end{cases}$  and  $g_{kw}$  is the interaction strength between the  $k$ th component and the solid. The external body force  $\mathbf{F}_3^k$  is simply given by

$$\mathbf{F}_3^k = m^k n^k \mathbf{g}^k \quad \text{Eq. 22,}$$

where  $m^k$  is the molecular mass and  $\mathbf{g}^k$  is the body force per unit mass. With Eq. 8 and Eq. 19- Eq. 22, the modified equilibrium molecular distribution can be calculated, and then the BGK operator can be used to update the LBM equation.

For the D3Q19 LBM model, one can obtain the momentum equation for the multiphase system using the Chapman-Enskog expansion on Eq. 8, Eq. 9, Eq. 19 and Eq. 20:

$$\begin{aligned} \frac{\partial \mathbf{u}}{\partial t} + \mathbf{u} \cdot \nabla \mathbf{u} = & -\frac{1}{\rho} \left\{ \nabla \left[ \frac{\Delta x^2}{2\Delta t^2} \sum_{k=1}^s (1-d_0) m^k n^k + 3\Delta x^2 \sum_{k=1}^s \sum_{k'=1}^s g_{kk'} \psi^k \psi^{k'} \right] + \sum_{k=1}^s m^k n^k \mathbf{g}^k \right\} + \\ & \left( \frac{\Delta x^2}{3\Delta t^2 \rho} \sum_{k=1}^s m^k n^k \tau^k - \frac{\Delta x^2}{6\Delta t} \right) \nabla^2 \mathbf{u}. \quad \text{Eq. 23} \end{aligned}$$

Comparing Eq. 23 with the incompressible Navier-Stokes equations, the expressions of pressure and kinematic viscosity can be obtained as:

$$p = \frac{\Delta x^2}{2\Delta t^2} \sum_{k=1}^s (1-d_0) m^k n^k + 3\Delta x^2 \sum_{k=1}^s \sum_{k'=1}^s g_{kk'} \psi^k \psi^{k'}, \quad \text{Eq. 24}$$

$$\nu = \frac{\Delta x^2}{3\Delta t^2 \rho} \left( \sum_{k=1}^s m^k n^k \tau^k - \frac{\Delta t}{2} \rho \right). \quad \text{Eq. 25}$$

The expression of pressure and viscosity can be obtained similarly for the D2Q9 LBM model. Notice that the kinematic viscosity is composed of two parts. The first one is the effect of intermolecular collisions and the second one is a numerical viscosity introduced by the FD scheme. Now, we need to determine the value of  $d_0$ . Consider a single-

component system. When  $n \rightarrow 0$ , from Eq. 24 we have  $p \approx \frac{\Delta x^2}{2\Delta t^2} (1-d_0) m^1 n^1$  (Shan, X. and Doolen, G., 1996). In this case, the fluid is essentially an ideal gas, and we have the equation of state as  $p = n^1 RT$ . In order to make the two equations of state consistent, one chooses

$$d_0 = 1 - RT \frac{2\Delta t^2}{\Delta x^2 m^1}. \quad \text{Eq. 26}$$

Although Shan-Chen's model has several limitations, it is relatively easy to implement and is able to capture many fundamental physical properties of multiphase flow. Therefore, Shan-Chen's model is used in our study.

### 1.2.3. Free-Energy Model

Different from other models that are “bottom-up”, i.e. starting with intermolecular interactions, the free-energy model employs a “top-down” strategy dealing with the free energy of the entire system. First proposed by Swift *et al.* (Swift, M. *et al.*, 1995), it has been improved by Zheng *et al.* (Zheng, H. *et al.*, 2006). In this section, we will follow the terminology and method described in Zheng's paper.

In a two phase system, one can define the total density  $n = n^1 + n^2$  and order index  $\phi = \frac{n^1 - n^2}{2}$ . The two macroscopic variables are governed by the Navier-Stake equations and the Cahn-Hilliard equation (Zheng, H. *et al.*, 2006):

$$\frac{\partial n}{\partial t} + \nabla \cdot (n\mathbf{u}) = 0, \quad \text{Eq. 27}$$

$$\frac{\partial (n\mathbf{u})}{\partial t} + \nabla \cdot (n\mathbf{u}\mathbf{u}) = -\nabla (p_0 + \phi\xi) + \xi\nabla\phi + \mu\nabla^2\mathbf{u} + \mathbf{F}, \quad \text{Eq. 28}$$

$$\frac{\partial \phi}{\partial t} + \nabla \cdot (\phi\mathbf{u}) = \theta_M \nabla^2 \xi, \quad \text{Eq. 29}$$

where  $p_0$  is the hydrodynamic pressure,  $\mu$  is the dynamic viscosity,  $\mathbf{F}$  is the body force,  $\theta_M$  is the phase mobility and  $\xi$  is the chemical potential. To solve Eq. 27- Eq. 29, Zheng *et al.* proposed two LBM equations (Zheng, H. *et al.*, 2006),

$$f_i(\mathbf{x} + \mathbf{e}_i\Delta t, t + \Delta t) = f_i(\mathbf{x}, t) + \left(1 - \frac{1}{2\tau_n}\right) \frac{\omega_i}{c_s^2} \left[ (\mathbf{e}_i - \mathbf{u}) + \frac{(\mathbf{e}_i \cdot \mathbf{u})}{c_s^2} \|\mathbf{e}_i\| \right] \cdot (\xi\nabla\phi + \mathbf{F})\Delta t - \frac{f_i(\mathbf{x}, t) - f_i^{eq}(\mathbf{x}, t)}{\tau_n}, \quad \text{Eq. 30}$$

$$g_i(\mathbf{x} + \mathbf{e}_i\Delta t, t + \Delta t) = g_i(\mathbf{x}, t) + \left(1 - \frac{1}{\tau_\phi + 0.5}\right) \left( g_i(\mathbf{x} + \mathbf{e}_i\Delta t, t) - g_i(\mathbf{x}, t) \right) - \frac{g_i(\mathbf{x}, t) - g_i^{eq}(\mathbf{x}, t)}{\tau_\phi},$$

**Eq. 31**

where  $f_i$  and  $g_i$  are the distribution of  $n$  and  $\phi$  in direction  $\mathbf{e}_i$ , respectively, and  $\tau_\phi$  is the relaxation time of diffusion, which is related to  $\theta_M$  by



$$\theta_M = \frac{\Gamma(\tau_\phi - 0.5)}{(\tau_\phi + 0.5)^2} \text{ with } \Gamma \text{ being a constant. From the Chapman-Enskog expansion, it is}$$

demonstrated that Eq. 30 and Eq. 31 can recover Eq. 27- Eq. 29 to second order (Zheng, H. *et al.*, 2006).

To obtain the expression of chemical potential  $\xi$ , the free energy functional is calculated with the expression (Zheng, H. *et al.*, 2006):

$$U = \int_V dV \left[ \lambda(\phi) + \frac{\kappa}{2} (\nabla \phi)^2 + \frac{n \ln n}{3} \right] = \int_V E dV, \quad \text{Eq. 32}$$

where  $\lambda$  is the bulk free energy density,  $\kappa$  is the coefficient controlling the interface strength and  $E$  is the free energy density. In the case of two phase flow,  $\lambda(\phi)$  has only two minima representing the two stable phases in the system. Usually, it is expressed as:

$$\lambda(\phi) = A(\phi^2 - \phi^{*2})^2. \quad \text{Eq. 33}$$

Therefore, the chemical potential is given by:

$$\lambda(\phi) = \frac{dE}{d\phi} = \frac{\partial E}{\partial \phi} - \nabla \cdot \frac{\partial E}{\partial (\nabla \phi)} = A(4\phi^3 - 4\phi^{*2}\phi) - \kappa \nabla^2 \phi. \quad \text{Eq. 34}$$

Eq. 25 can be easily evaluated through a central-difference scheme.

In order to account for solid wettability, an additional term for solid-fluid surface energy should be added to the total free energy of the system. Details are given in the publication by Niu *et al.* (Niu, X. *et al.*, 2007).

#### 1.2.4. Mean-Field Model

Using Enskog's theory and the mean-field approximation, the Boltzmann Equation can be written as (He, X *et al.*, 1999),

$$\frac{\partial f}{\partial t} + \mathbf{v} \cdot \frac{\partial f}{\partial \mathbf{x}} = -\frac{f - f^{eq}}{\tau \Delta t} + \frac{(\mathbf{v} - \mathbf{u}) \cdot (\mathbf{F} + \mathbf{G})}{nRT} f^{eq} \quad \text{Eq. 35}$$

where  $\mathbf{G}$  is the effective intermolecular force.  $\mathbf{G}$  can be further expressed as (He, X *et al.*, 1999)

$$\mathbf{F} = -\nabla \psi + \kappa n \nabla \nabla^2 n \quad \text{Eq. 36}$$

where  $\psi(n)$  is a measure of discrepancy between non-ideal and ideal gases:

$$\psi(n) = p - nRT, \quad \text{Eq. 37}$$

and  $\kappa$  is a coefficient controlling the surface tension. Now define a new variable  $g$  as (He, X *et al.*, 1999):

$$g = fRT + \psi(n)\Gamma(0), \quad \text{Eq. 38}$$

where  $\Gamma(\mathbf{u})$  is the Maxwell-Boltzmann distribution:

$$\Gamma(\mathbf{u}) = \frac{1}{2\pi RT} e^{-\frac{(\mathbf{v}-\mathbf{u})^2}{2RT}}. \quad \text{Eq. 39}$$

The equilibrium distribution of  $f$  is as simple as

$$f^{eq} = n\Gamma(\mathbf{u}). \quad \text{Eq. 40}$$

From Eq. 35, it is straightforward to obtain

$$\frac{Dg}{Dt} = RT \frac{Df}{Dt} + \Gamma(0) \frac{D\psi(n)}{Dt}. \quad \text{Eq. 41}$$

For incompressible flow, the material derivative holds, so that

$\frac{dn}{dt} = \frac{\partial n}{\partial t} + (\mathbf{u} \cdot \nabla)n = 0$ . Incorporating Eq. 36, Eq. 38 and Eq. 41, the evolution equation of  $g$  is expressed as (He, X *et al.*, 1999):

$$\frac{Dg}{Dt} = -\frac{g - g^{eq}}{\tau \Delta t} + (\mathbf{v} - \mathbf{u}) \cdot \left[ \Gamma(\mathbf{u}) (\kappa n \nabla^2 n + \mathbf{G}) - (\Gamma(\mathbf{u}) - \Gamma(0)) \nabla \psi(n) \right] \quad \text{Eq. 42}$$

where  $g^{eq} = nRT\Gamma(\mathbf{u}) + \psi(n)\Gamma(0)$ . Applying the explicit FD scheme to Eq. 35 and 40 leads to the LBM equation for mean-field model.

### 1.3. Boundary Conditions

#### 1.3.1. Fluid Boundary Condition

At the fluid boundary lattice points  $\mathbf{x}$ , denote velocities  $\mathbf{e}_p$  with the direction pointing inward from undefined lattice points, i.e., out of the simulation area. Therefore, the value of  $f_p(\mathbf{x} - \mathbf{e}_i \Delta t, t - \Delta t)$  is undefined. Chang *et al.* assumed that the following relation holds (Chang, C. *et al.*, 2009):

$$f_p(\mathbf{x}, t + \Delta t) = f_p(\mathbf{x}, t) + \frac{\omega_p \Delta t}{\Delta x_s} \mathbf{e}_i \cdot \mathbf{Q} \quad \text{Eq. 43}$$

where  $\mathbf{Q} = (Q_x, Q_y)^T$  is the corrector vector to the distribution on the boundary, and  $\omega_p$  is the fraction of the distribution for the  $p$  th velocities at  $\mathbf{u} = \mathbf{0}$ . In the D2Q9 scheme defined in Section 1.1.1, suppose  $f_4, f_7, f_8$  are unknown at the boundary lattice points prior to the streaming step, which is the case when the boundary lies in the  $x$  direction, then the molar density and momentum can be expressed as

$$n = f_0 + f_1 + f_2 + f_3 + (f_4^* - \omega_4 Q_y) + f_5 + f_6 + [f_8^* + \omega_8 (Q_x - Q_y)], \quad \text{Eq. 44}$$

$$nu_x = f_1 - f_3 + f_5 - f_6 - [f_7^* - \omega_7 (Q_x + Q_y)] + [f_8^* + \omega_8 (Q_x - Q_y)], \quad \text{Eq. 45}$$

$$nu_y = f_2 - (f_4^* - \omega_4 Q_y) + f_5 + f_6 - [f_7^* - \omega_7 (Q_x + Q_y)] - [f_8^* + \omega_8 (Q_x - Q_y)]. \quad \text{Eq. 46}$$

Here the variables with star refer to the value prior to streaming. If the velocity is specified on the boundary, i.e.  $\mathbf{u} = (u_x, u_y)^T$  is known, the equations can be readily solved as (Chang, C. *et al.*, 2009):

$$n = \frac{f_0 + f_1 + f_3 + 2(f_2 + f_5 + f_6)}{1 + u_y}, \quad \text{Eq. 47}$$

$$f_4 = f_4^* - \frac{2}{3}nu_y + \frac{2}{3}(f_2 - f_4^* + f_5 - f_7^* + f_6 - f_8^*), \quad \text{Eq. 48}$$

$$f_7 = f_7^* - \frac{1}{2}nu_x - \frac{1}{6}nu_y + \frac{1}{2}(f_1 - f_3) + \frac{1}{6}(f_2 - f_4^*) + \frac{2}{3}(f_5 - f_7^*) - \frac{1}{3}(f_6 - f_8^*), \quad \text{Eq. 49}$$

$$f_8 = f_8^* + \frac{1}{2}nu_x - \frac{1}{6}nu_y - \frac{1}{2}(f_1 - f_3) + \frac{1}{6}(f_2 - f_4^*) - \frac{1}{3}(f_5 - f_7^*) + \frac{2}{3}(f_6 - f_8^*). \quad \text{Eq. 50}$$

If any two of  $n, u_x$  and  $u_y$  are given, the linear system of Eq. 47- Eq. 50 can be solved and the molecular distribution, density, and macroscopic velocity can all be determined. It is reported that this scheme generates a smoother pressure transition near the boundary when compared with the traditional velocity boundary<sup>1</sup>. Usually, one of  $u_x$  and  $u_y$  is fixed at 0. Additionally, we either fix  $n$  to produce a pressure boundary condition from the equation of state  $p = p(n)$ , or we fix the other velocity component to produce a velocity boundary condition.

### 1.3.2. Solid Boundary Condition

---

<sup>1</sup> Personal communication with Xiao-Yan Shi, graceshi@udel.edu, Department of Mechanical Engineering, University of Delaware, Newark, DE 19716, USA

The most widely used boundary condition on solid wall lattice points is the bounce-back BC which implies that molecules streaming towards the wall lattice points will bounce back in the opposite direction during the next time step (Cornubert, R. *et al.*, 1992). Consider a wall lattice points located at  $\mathbf{x}$  and its adjacent fluid lattice points  $\mathbf{x} - \mathbf{e}_i \Delta t$ . Denote  $\mathbf{e}_j = -\mathbf{e}_i$ . Then after the streaming step, we have

$$f_i(\mathbf{x}, t) = f_i^*(\mathbf{x} - \mathbf{e}_i \Delta t, t). \quad \text{Eq. 51}$$

To perform the bounce-back BC, we prescribe that

$$f_j(\mathbf{x}, t) = f_i(\mathbf{x}, t). \quad \text{Eq. 52}$$

In general, the accuracy of the bounce-back scheme is first order. It is also proved that if the physical boundary is located in the mid-point of  $\mathbf{x}$  and  $\mathbf{x} - \mathbf{e}_i \Delta t$ , second-order accuracy can be achieved (Cornubert, R. *et al.*, 1992). Therefore, the assignment of wall or fluid lattice points should place the mid-point as close to the physical boundary to possible. Although other schemes claim to have higher order of accuracy for arbitrary boundary geometry, this advantage is not justifiable given the resolution of the pore space available for us. Therefore, the bounce-back scheme is implemented in our study.

#### 1.4. Parallel Computing

As described in Section 1.1 and 1.2, one of the most significant advantages of LBM is that all the computations are between neighboring lattice points. This feature qualifies LBM as a perfect candidate for parallel computing. The unusually large number of variable associated with LBM further adds to the need for parallel computing. Our program is based on the one developed by Q. Kang and used in his published work (Kang, Q. *et al.*, 2002) (Kang, Q. *et al.*, 2005). The program is written in FORTRAN with the Message Passing Interface (MPI) (Gropp, W. *et al.*) to parallelize the LBM program, and runs on a SUN cluster with Linux as Operating System (OS).

In our program, the simulation area is evenly divided into rectangular subareas as devised in Q. Kang's original program (Kang, Q. *et al.*, 2005). Each subarea is calculated by a single CPU. There are two operations requiring communication between CPUs. The first one is the streaming of the molecular distribution at the boundary nodes of a subarea to its neighboring subarea. The other one is calculating the forces on boundary nodes imposed by a neighboring subarea. All of the 3D models are simulated with parallel computing. We used 80 Intel 2.26GHz CPUs for the parallel simulations.

## Chapter 2

### 2. Results

#### 2.1. Hele-Shaw Flow

Hele-Shaw flow is defined as the flow between two parallel infinite plates with very low Reynolds numbers. Fluid flow in saturated porous media usually takes place in the same range of Reynolds numbers as Hele-Shaw flow. When a low-viscosity fluid invades a higher-viscosity fluid, fluid fingers can be observed. A fluid finger is a slug of fluid within another fluid. Figure 1 is a schematic illustration of Hele-Shaw fingering in a 2D channel. In Figure 1,  $W$  and  $T$  are finger width and length,  $L$  and  $H$  are the channel width and length, and  $S$  is the wetting distance of phase 1. Using boundary element analysis, Halpern and Gaver (Halpern, D. and Gaver, D., 1994) obtained an empirical relation between the dimensionless finger width  $\frac{W}{H}$  and the capillary number  $Ca$  :

$$\frac{W}{H} = 1 - 0.417 \left( 1 - e^{-1.69 Ca^{0.5025}} \right). \quad \text{Eq. 53}$$

The capillary number is  $Ca$  defined by:

$$Ca \equiv \frac{u_t \rho_2 \nu_2}{\sigma}. \quad \text{Eq. 54}$$

where  $u_t$  is the tip velocity of the finger,  $\rho_2, \nu_2$  are the density and kinematic viscosity of the displaced phase, and  $\sigma$  is the surface tension between two phases. In addition, the viscosity ratio  $M = \frac{\nu_1}{\nu_2}$  has a significant effect on the fingering pattern (Kang, 2002). We

now use the D2Q9 LBM scheme described earlier to study the effect of the flow rate, viscosity, wettability, and density on the fingering pattern, and we validate the results with Eq. 53.

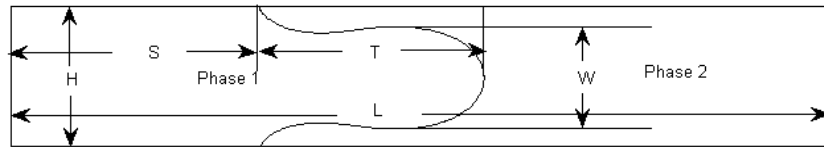


**Figure 1 Schematic Illustration of Fingering Channel**

In this simulation, the grid size is  $400 \times 66$ . The bounce-back boundary condition is applied on the two long sides of the rectangular region. Initially, the first 50 columns of the lattice cells are occupied by phase 1 with the rest occupied by phase 2. The initial

densities of both phases are  $n_0^i$  and  $n_0^i$ . In order to be consistent with the model studied by Halpern and Gaver (Halpern, D. and Gaver, D., 1994), we impose the Poiseuille velocity distribution at the inlet and outlet of the channel with maximum velocity  $u_0$ .

All parameters in this scenario are scaled as follows.

1. Length is scaled as  $l = \frac{l}{\Delta x}$ ;
2. Time is scaled as  $t = \frac{t}{\Delta t}$ ;
3. Mass is scaled as  $m = \frac{m}{m^1}$
4. Density of the  $i$  th phase is scaled as  $n = \frac{n}{n^i}$

In addition, we choose  $d_0 = \frac{1}{3}$  and assume that both phases have equal initial molecular density. The fluid-fluid interaction strengths are fixed at  $g_{12} = 0.25$ ,  $g_{11} = g_{22} = 0$ . The fluid-solid interaction strengths are related such that  $g_{1w} = g_{2w}$  with  $n^w$  assigned as 1. From the bubble test, the interface tension is obtained as  $\sigma = 0.11562$ . We repeat the simulation with different parameters. Table 1 shows the parameters for each simulation.

Simulation #	$v_1$	$v_2$	$m^2$	$u_0$	$g_{1w}$	$\Delta t$
1	0.333	0.333	1	0.01	0	5000
2	0.333	0.333	1	0.05	0	1000
3	0.333	0.333	1	0.1	0	500
4	0.083	0.333	1	0.01	0	5000
5	0.083	0.333	1	0.05	0	1000
6	0.083	0.333	1	0.1	0	500
7	0.033	0.333	1	0.01	0	5000

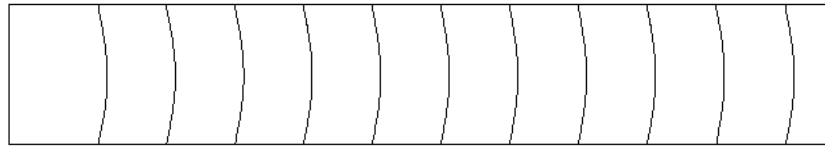
8	0.033	0.333	1	0.05	0	1000
9	0.033	0.333	1	0.1	0	500
10	0.033	0.333	1	0.1	0.03	500
11	0.033	0.333	1	0.1	-0.03	500
12	0.033	0.333	0.6	0.1	0	500
13	0.033	0.333	1.4	0.1	0	500

**Table 1 Parameter Option for Simulation**

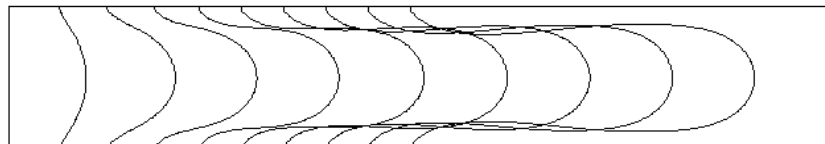
### 2.1.1. Effect of $M$

Figures 2-4 shows the evolution of the interface for  $M = 1, 4$  and  $10$ . For a small velocity  $u_0 = 0.01$ , the interface is very stable for all  $M$ . For a larger driving velocity  $u_0 = 0.05$ , fingers form with  $M = 1, 4$ , but  $M = 10$ . For the velocity  $u_0 = 0.1$ , fingers form with  $M = 4, 10$ . With  $M = 10$ , the interface is not stable yet the finger is not formed within the channel. For  $u_0 = 0.05$ , the finger forms faster for smaller  $M$ . On the other hand, for  $u_0 = 0.1$ , the finger forms is earlier for larger  $M$ . A similar study has been done by Kang *et al.* (Kang, Q. *et al.*, 2002). Values of the parameters used in our simulations are the same as in Kang's paper. Interestingly, the interface evolutions agree well with results in Kang's paper, except that Figure 2(b) and Figure 4(b) were swapped in Kang's paper.

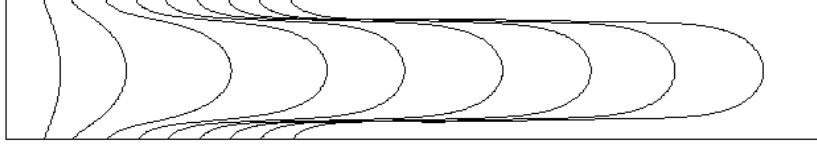
From simulation 1-simulation 9, it is clear that the viscosity ratio  $M$  has a significant effect on the formation of fingers in Hele-Shaw flows. However, contrary to our intuition, there is no monotonous dependence of whether the finger will form and when it begins to form. More simulations are needed to find out the condition for the onset of fluid fingering.



(a)



(b)

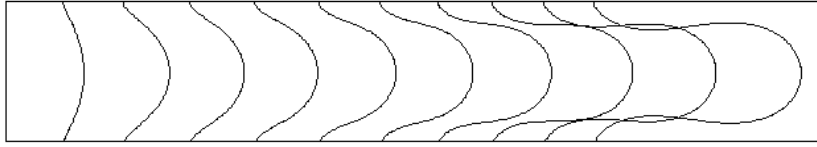


(c)

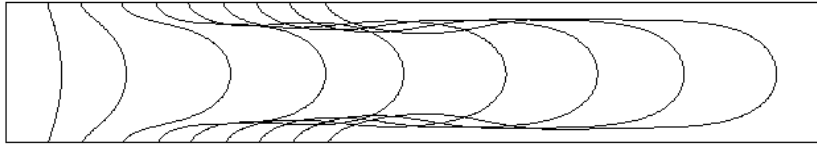
**Figure 2 Interface Evolutions for  $M = 1$  : (a) Simulation 1, (b) Simulation 2, and (c) Simulation 3**



(a)

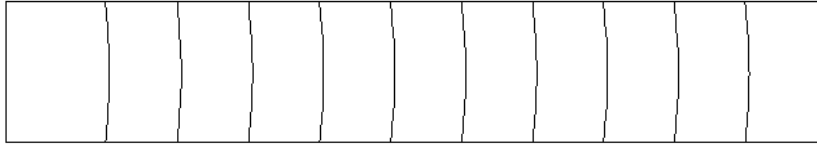


(b)



(c)

**Figure 3 Interface Evolutions for  $M = 4$  : (a) Simulation 4, (b) Simulation 5, and (c) Simulation 6**

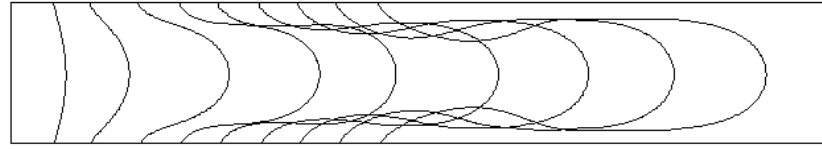


(a)





(b)

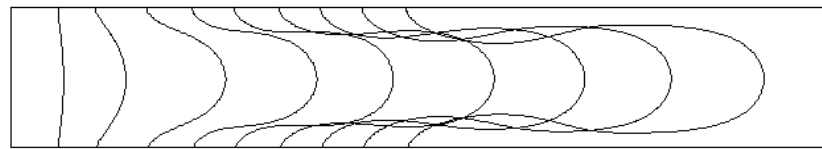


(c)

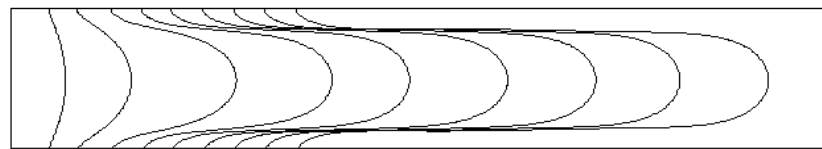
**Figure 4 Interface Evolutions for  $M = 10$  : (a) Simulation 7, (b) Simulation 8, and (c) Simulation 9**

### 2.1.2. Effect of $g_{1w}$

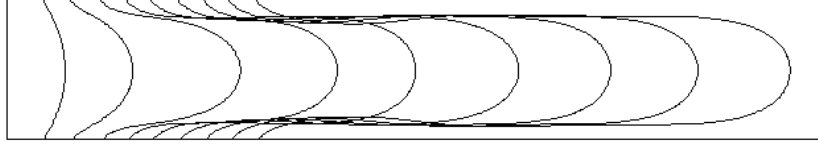
Figure 5 shows the evolution of the interface with  $g_{1w} = -0.03, 0$ , and  $0.03$ , while  $M$  is fixed at 1. and  $u_0$  is fixed to 0.1. From Figure 5, we can see that as  $g_{1w}$  decreases, the tip of the interface moves slower and the wetting distance increases. This phenomenon occurs because, with a higher wettability, phase 1 has preference to the wall, and it tends to displace phase 2 along the walls instead of penetrating into the bulk of phase 2. The wettability of phase 1 also has an impact on the shape of the finger. Comparing Figure 5(a), with Figure 5(c), a significant “bottle neck” can be found in the finger in Figure 5(a) and the curvature of the “bottle neck” increases with time. Further study is needed to determine whether the “bottle neck” will lead to detachment in later stages.



(a)



(b)

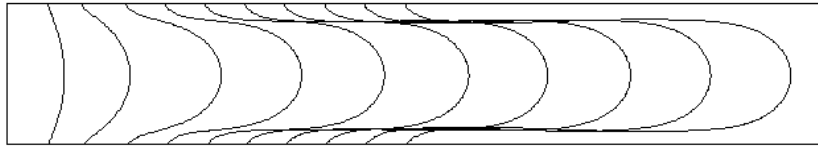


(c)

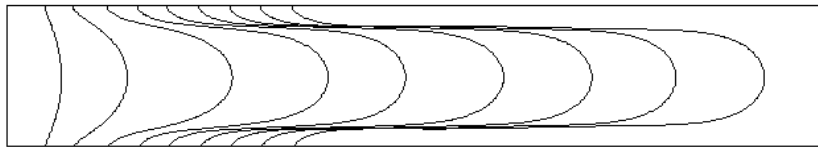
**Figure 5 Interface Evolutions with  $g_{1w} = -0.03, 0$  and  $0.03$ : (a) Simulation 10, (b) Simulation 3, and (c) Simulation 11**

### 2.1.3. Effect of $m^2$

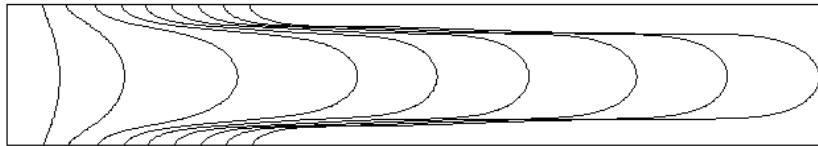
Figure 6 shows evolution of the interface with  $m^2 = 0.6, 1$ , and  $1.4$ , while  $M$  is fixed to 1 and  $u_0$  is fixed at 0.1. From Figure 5, we can see that as the molecular mass of phase 1 increases, the tip of the interface moves faster, and the wetting distance increases at a lower rate. Also, although the interface is unstable, a finger does not form with  $m^2 = 1.4$ . Comparing the shape of the interface in Figure 6(a) with that in Figure 6(c), it can be concluded that as  $m^2$  increases, it takes longer to form a finger. However, these conclusions cannot be generalized to fluids with different mass density, since the mass density is also determined by the molar density of fluid, not only the molecular mass.



(a)



(b)



(c)

**Figure 6(a)-(c) Interface Evolutions with  $m^2=0.6, 1$  and  $1.4$ : (a) Simulation 12, (b) Simulation 3, and (c) Simulation 13**

#### 2.1.4. Comparison with Empirical Solutions

Out of the 13 simulations we conducted, there are 7 simulations in which recognizable fingers form. Table 2 shows the dimensionless width of the fingers and the result from Halpern-Gaver's empirical formula. According to Table 2, the simulation results agree well with the theoretical prediction except for Simulation 5, where the simulated finger width is less than the theoretical value. Considering the late formation of the finger in Simulation 5, the discrepancy between the simulated and theoretical result can be explained by the fact that the finger in Simulation 5 has not reached steady state.

By comparing the simulation results with theoretical predictions, the Shan-Chen's model is proven adequate in modeling multiphase Helen-Shaw flow for a reasonably wide range of parameters.

Simulation #	$Ca$	$\frac{W}{H}$	$\frac{W}{H}$ by H-G Formula
2	0.2313	0.7621	0.7685
5	0.2403	0.7082	0.7657
6	0.2607	0.7770	0.7595
9	0.2599	0.7791	0.7597
10	0.2444	0.7611	0.7644
11	0.2603	0.7800	0.7596
12	0.1355	0.7802	0.8076

**Table 2 Simulated and Theoretical Finger Widths**

## 2.2. Single-Phase Flow in Three Dimensions

In single-phase flow simulation, we study the steady-state flow in glass beads packs generated by Finney (Finney, J., 1970). Figure 7 is the 3D image of the glass beads packing. Various  $\Delta p$  values are applied at the inlet, and the flow rate at the outlet is measured after the flow reaches steady state. Since only one phase is present, it is not necessary to consider wettability issues. Similar to Section 2.1, we set  $g_{11} = 0$  and  $\tau = 1.5\Delta t$ . As a result, we actually simulate the flow of an ideal gas through the porous media. The lattice size of the model is  $\Delta x = 5.3333 \times 10^{-5} \text{m}$ . The grid has

150×150×150 voxels. We compute the permeability of the bead pack under different pressure gradients and compare the computations with the experimental results. The permeability  $k$  is defined using Darcy's law:

$$q = -\frac{kA\Delta p}{\mu L}. \quad \text{Eq. 55}$$

where  $q$  is the flow rate,  $A$  is the cross-section area,  $L$  is the distance between inlet and outlet, and  $\Delta p$  is the pressure difference between inlet and outlet. Since the pack is cubic, we have  $\frac{A}{L} = 150\Delta x$ . Substituting Eq. 24 and Eq. 25 into Eq. 55 and choosing  $d_0 = \frac{1}{3}$ , we have

$$\frac{\bar{u}}{\frac{\Delta x}{\Delta t}} = -\frac{1}{150\left(\frac{\tau}{\Delta t} - \frac{1}{2}\right)} \cdot \frac{\Delta n}{n_0} \cdot \frac{k}{\Delta x^2}, \quad \text{Eq. 56}$$

where  $\bar{u}$  is defined by  $\bar{u} = \frac{q}{A}$  and  $\Delta n$  is the molecular density difference between the inlet and outlet. Thus, the dimensionless permeability  $\frac{k}{\Delta x^2}$  can be expressed in terms of the dimensionless number  $\frac{\bar{u}}{\frac{\Delta x}{\Delta t}}$ ,  $\frac{\tau}{\Delta t}$  and  $\frac{\Delta n}{n_0}$ . Table 3 lists the effective permeability, flow rate, and molecular density difference of each simulation and all the dimensionless numbers.

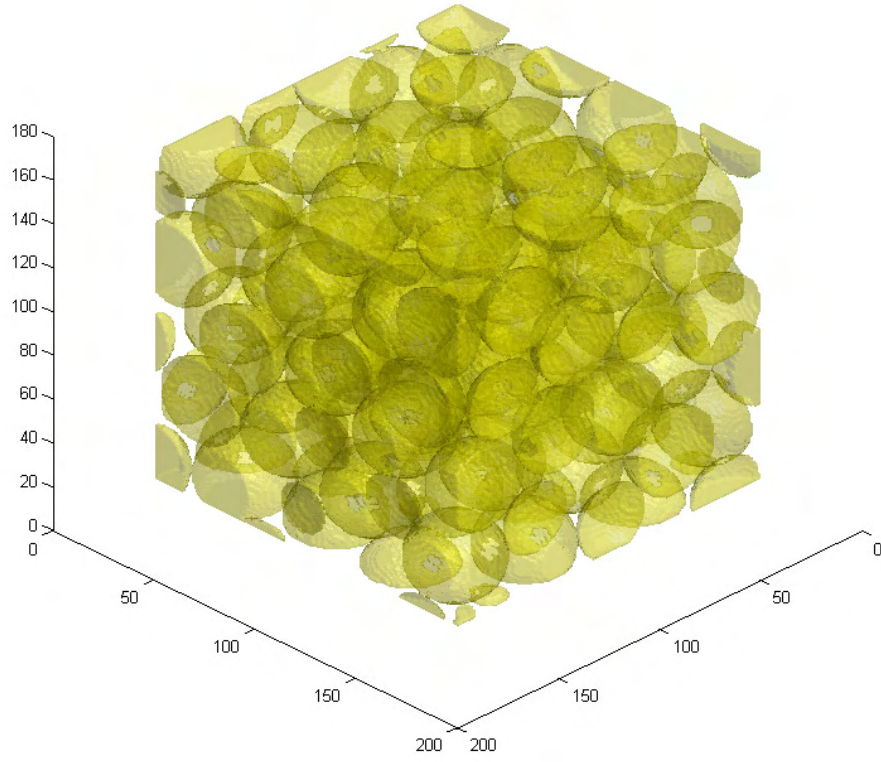


**Figure 7 Glass Bead Pack: Blue for the Glass Beads**

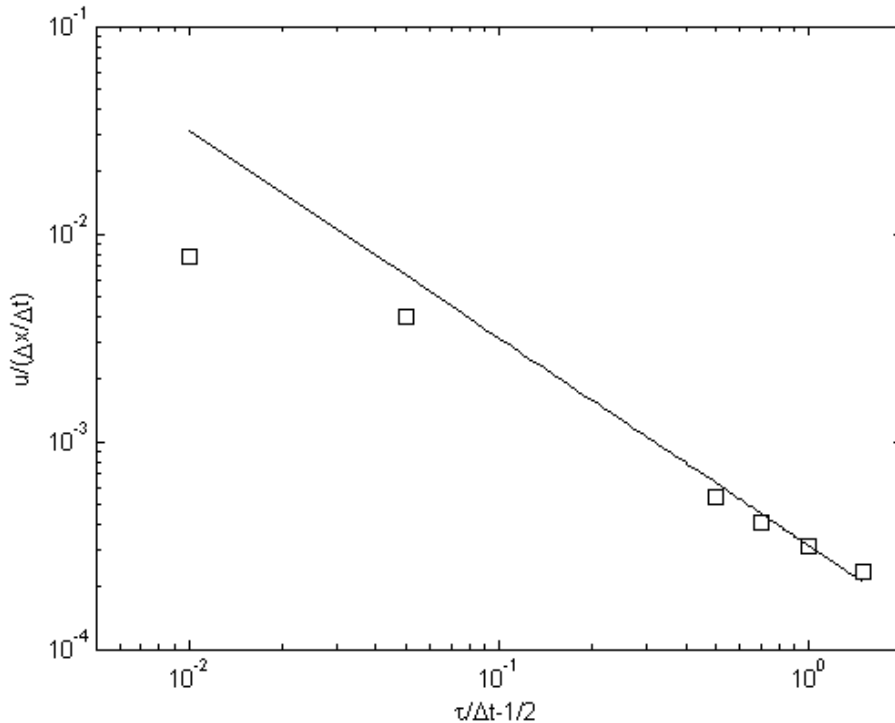
Simulation #	$\frac{\bar{u}}{\frac{\Delta x}{\Delta t}}$	$\frac{\tau}{\Delta t} - \frac{1}{2}$	$\frac{\Delta n}{n_0}$	$\frac{k}{\Delta x^2}$
1	$2.3472 \times 10^{-4}$	1.5	0.05	1.0562
2	$4.1091 \times 10^{-4}$	0.7	0.05	0.8629
3	$5.4420 \times 10^{-4}$	0.5	0.05	0.8163
4	$3.9969 \times 10^{-3}$	0.05	0.05	0.5995
5	$7.8147 \times 10^{-3}$	0.01	0.05	0.2344

6	$6.2122 \times 10^{-5}$	1	0.01	0.9318
7	$3.1153 \times 10^{-4}$	1	0.05	0.9346
8	$6.2308 \times 10^{-4}$	1	0.1	0.9346
9	$1.2457 \times 10^{-3}$	1	0.2	0.9343
10	$1.8680 \times 10^{-3}$	1	0.3	0.9340
11	$4.3376 \times 10^{-3}$	1	0.7	0.9295

**Table 3 Dimensionless Parameters for Single Phase Simulations**

Figure 8 shows the simulated relationship between  $\frac{\bar{u}}{\frac{\Delta x}{\Delta t}}$  and  $\frac{\tau}{\Delta t} - \frac{1}{2}$  as well as  $\frac{\Delta n}{n_0}$ .

Here the solid line represents a permeability equal to  $0.9437 \Delta x^2$  as given by the experimental data. We can see from Table 3 and Figure 8 that when the dimensionless kinematic viscosity  $\frac{\tau}{\Delta t} - \frac{1}{2}$  and the density variation  $\frac{\Delta n}{n_0}$  take values in a moderate range, the simulated permeability agrees well with the experimental result. However, when the viscosity is small, or the density variations are large, the flow pattern displays instabilities, and the effective permeability deviates from the experimental results.



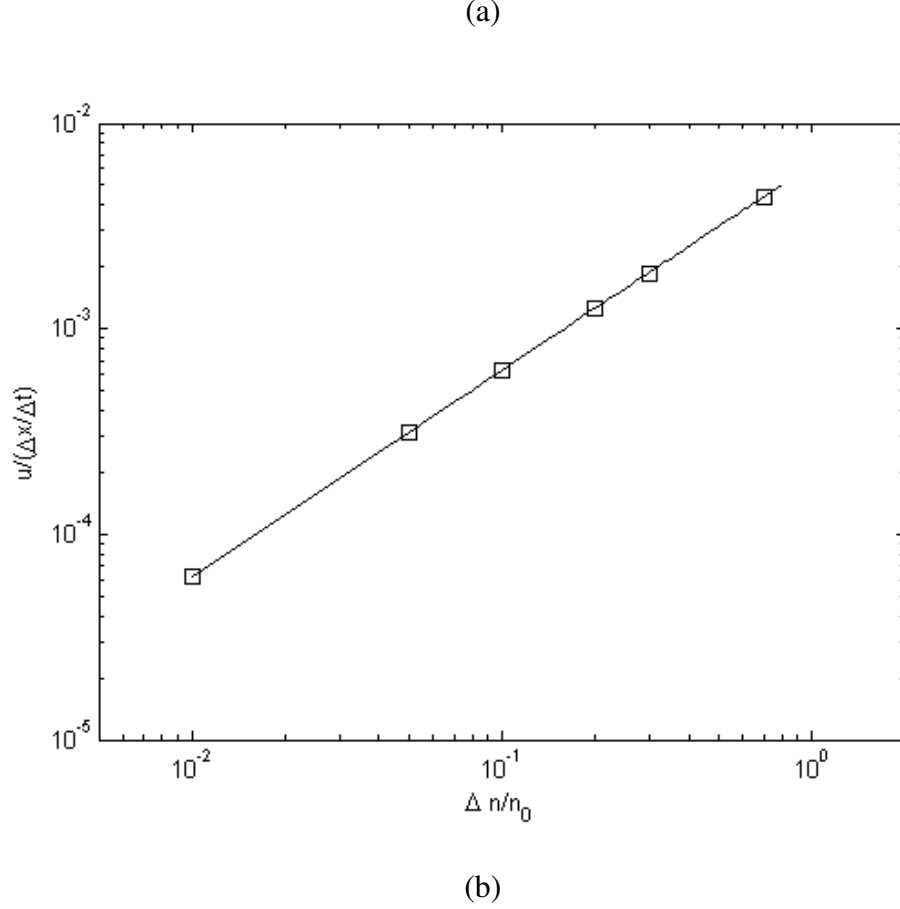


**Figure 8 Relation between Dimensionless Parameters:**

$$(a) \frac{\bar{u}}{\frac{\Delta x}{\Delta t}} \text{ vs. } \frac{\tau}{\Delta t} - \frac{1}{2}, (b) \frac{\bar{u}}{\frac{\Delta x}{\Delta t}} \text{ vs. } \frac{\Delta n}{n_0}$$

### 2.3. Simulating CO<sub>2</sub>-Water Flow in Sandstone

Herem we simulate the process of CO<sub>2</sub> imbibition and drainage in sandstone pre-saturated with saline water based on a digitized 3D image of a rock sample.

#### 2.3.1. Model Description

We use the D3Q19 LBM model to simulate the CO<sub>2</sub>-water binary system in sandstone. The 3D image of Fontainebleau sandstone segment is obtained from micro-CT scanning (Krzikalla, F. *et al.*, 2010). The resolution of the imaging is 40×40×40 voxels with lattice spacing  $\Delta x = 1.404 \times 10^{-5}$  m. The porosity of the sandstone is 15.9%, and the effective permeability is calculated to be 1.89D from single-phase flow simulation. The pore structure of the sandstone is shown in Figure 9.

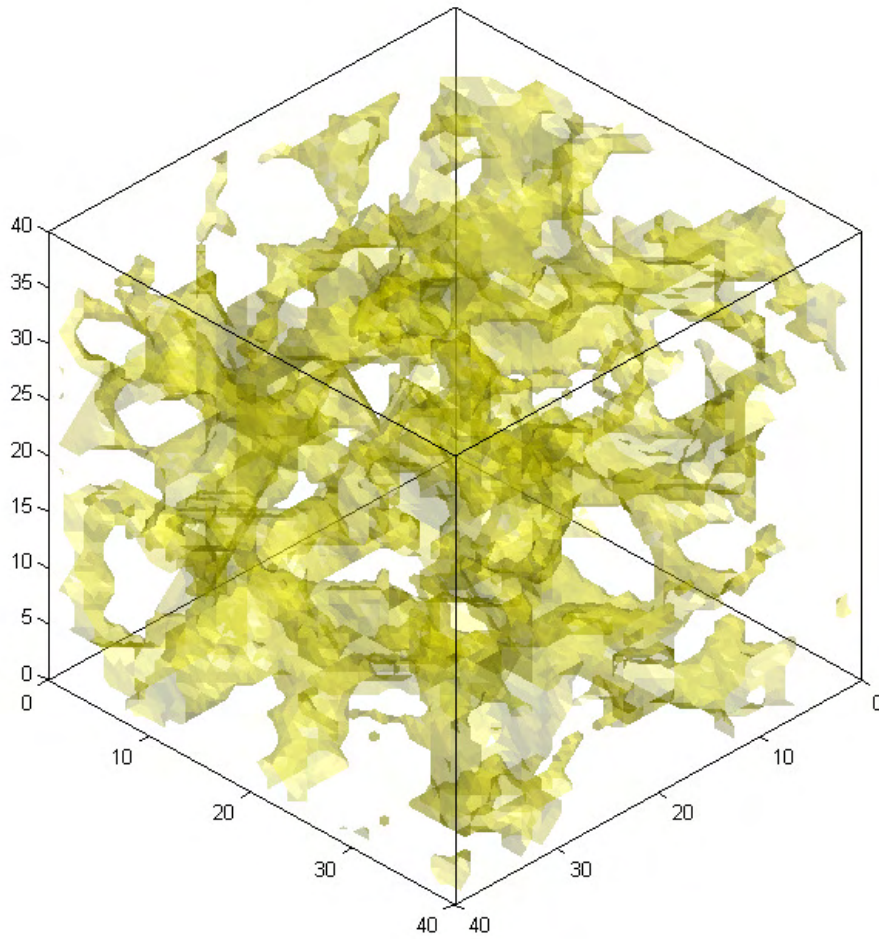


**Figure 9 Pore Structure of the Sandstone: Yellow for the Pore Space and White for the Rock**

### ***2.3.2. Parameter Calibration***

Although there are many publications on simulation of porous media flow using LBM, variables in most of them are usually expressed in dimensionless numbers. Therefore, it is difficult to relate the results in those publications to a physical model. To avoid such issues, all the variables are reported here in dimensional form. Thus, we can choose parameters in our model to simulate physical problems.

Now we consider a typical scenario in CO<sub>2</sub> sequestration. The injection depth is set to 1250m. At this depth, the ambient temperature is 41.25°C, and the pressure is 12.36MPa. For simplicity, we will use properties of pure water instead of saline water. Under these conditions, the physical properties of pure water and supercritical CO<sub>2</sub> are listed in Table 3 (NIST Chemistry WebBook).



	Water	Supercritical CO <sub>2</sub>
Molar Density (mol/m <sup>3</sup> )	55344	16239
Mass Density (kg/m <sup>3</sup> )	997.04	714.69
Dynamic Viscosity (μPa•s)	639.25	58.160

**Table 4 Physical Properties of Water and CO<sub>2</sub>**

We can see that although the density of supercritical CO<sub>2</sub> is of the same order as a typical fluid, the viscosity and sound of speed of CO<sub>2</sub> are close to the value of a typical gas. We denote supercritical CO<sub>2</sub> as phase 1 and water as phase 2. According to Eq. 24, the interaction strength  $g_{11}$  is given by:

$$g_{11} = \frac{1}{3\Delta x^2 \Psi^2(n^1)} (p - n^1 RT). \quad \text{Eq. 57}$$

Substituting values from Table 4 into Eq. 57, the values of the interaction strength are given as  $g_{11} = -4.8233 \times 10^7 \text{ J} \cdot \text{m} / \text{mol}^2$  and  $g_{22} = -1.8261 \times 10^7 \text{ J} \cdot \text{m} / \text{mol}^2$ . Both values are negative, indicating the force is attractive between molecules. Using a square root mixing rule, the interaction strength between two components  $g_{12}$  can be approximated by (Reid, R. *et al.*, 1987)

$$g_{12} = -\sqrt{g_{11} g_{22}}. \quad \text{Eq. 58}$$

In this way, the value of  $g_{12}$  is found to be  $-2.9678 \times 10^7 \text{ J} \cdot \text{m} / \text{mol}^2$ . The interfacial tension between supercritical CO<sub>2</sub> and saline water  $\sigma_{w-\text{CO}_2}$  is about 28mN/m (Chalbaud, C. *et al.*, 2009). A more rigorous way to obtain the value  $g_{12}$  is to perform a bubble test and find the value of  $g_{12}$  that yields the desired  $\gamma_{w-\text{CO}_2}$ . The value of  $n^w g_{w1}$  and  $n^w g_{w2}$  cannot be determined uniquely from available experiment data of the contact angle. Special experiments are needed to measure the interaction between the rock surface and the fluids.

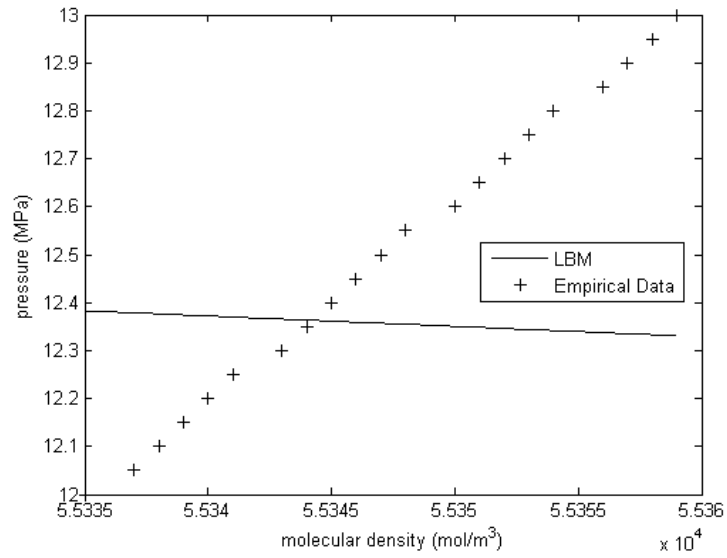
There is another method to determine the fluid-fluid interaction strength. It is well known that the speed of sound in a media can be calculated by:

$$c_s = \sqrt{\left(\frac{\partial p}{\partial \rho}\right)_{\text{isothermal}}} = \sqrt{\frac{C_p}{C_v} \left(\frac{\partial p}{\partial \rho}\right)_{\text{adiabatic}}}, \quad \text{Eq. 59}$$

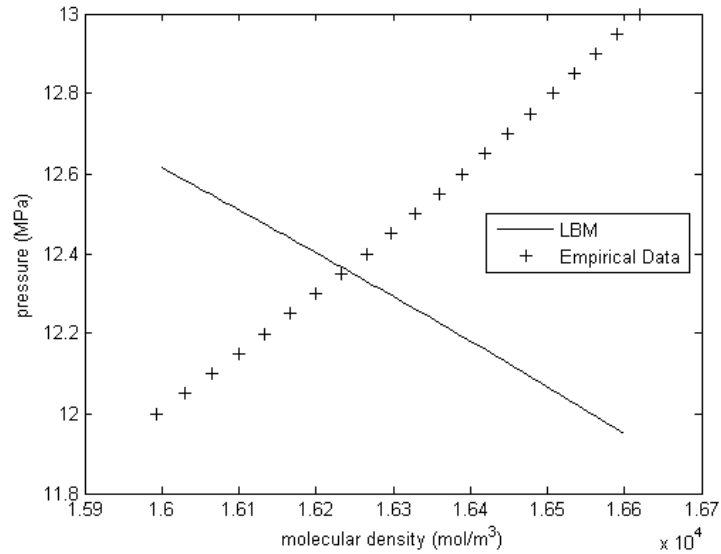
where  $C_v, C_p$  are the isochoric and isobaric heat capacity respectively. Notice that Shan-Chen's model is isothermal (He, 2002). Given these data (Chemistry WebBook), we can calculate the value of  $g_{11}$  from Eq. 24 and Eq. 26 as  $6.941 \times 10^7 \text{ J} \cdot \text{m} / \text{mol}^2$ , which have opposite sign compared with the result obtained in the previous calculation.

From Eq. 26, it is clear that the time step  $\Delta t$  is determined by  $\Delta x$  and  $d_0$ . Obviously, the value of  $d_0$  must be between 0 and 1 to guarantee a non-negative equilibrium distribution. If we choose  $d_0$  as  $\frac{1}{3}$  for  $\text{CO}_2$  as we did in the previous approach (Yuan, 2006) (Kang, 2002, 2005),  $\Delta t$  is given as  $3.3257 \times 10^{-8} \text{ s}$ . One can also infer from Eq. 26 that the lower limit of molecular mass of the model is  $2RT \frac{\Delta t^2}{\Delta x^2}$ . Considering that the molecular collision frequency is  $\sim 10^{12} \text{ s}^{-1}$  in liquids, this  $\Delta t$  is long enough to satisfy the ensemble average condition. However, it is still too short for many processes of interest. Now, we can calculate the relaxation time for water and  $\text{CO}_2$  as  $\tau^1 = (0.5 + 4.1189 \times 10^{-5}) \Delta t$  and  $\tau^2 = (0.5 + 3.2451 \times 10^{-4}) \Delta t$ .

The above-mentioned LBM parameters, however, are not feasible for numerical simulation. First, the equation of state of LBM is non-physical with these parameters. Figure 3 shows the pressure-density curve of  $\text{CO}_2$  and water. The curve obtained from Eq. 24 deviates far from the empirical result (Chemistry WebBook). The equation of state of LBM predicts that the pressure of  $\text{CO}_2$  or water decreases with the molecular density, which is nonphysical. Second, the kinematic viscosity of  $\text{CO}_2$  and water is so small that the corresponding relaxation times of both phases are extremely close to  $0.5 \Delta t$ , which will lead to numerical instability. Inspired by the idea of the similitude model frequently used in engineering test (Kline, S., 1965), we replace  $\text{CO}_2$  and water with "Virtual Fluid" (VF) I and II to facilitate the simulation. The physical properties of the "virtual fluids" are carefully tuned so that the fluids can be addressed adequately by the Shan-Chen model. Similitude analysis is then employed to scale results back to the actual model.



(a)



(b)

**Figure 10 Pressure-Density Curve: (a) CO<sub>2</sub>, (b) Water**

Since the geometry of the virtual model is the same as the original one, there is no issue of geometric similarity. It is well known that subsurface flow features significant viscous, pressure difference, and surface tension forces with negligible inertial force. As a result, the dynamic similarity requires that the actual model and the virtual one must have the same values for two dimensionless numbers. The first one is the ratio between the viscous force and the surface tension force

$$\Pi = \frac{\mu u}{\sigma} = \text{const.} \quad \text{Eq. 60}$$

The second one is the Stokes number measuring the ratio between the pressure force and the viscous force

$$Stk = \frac{\Delta p \Delta x}{\mu u} = \text{const.} \quad \text{Eq. 61}$$

In the case that the flow is driven by body forces such as gravity, the Stokes number is replaced by the Galilei number measuring the ratio between gravity and viscous forces

$$Ga = \frac{g \Delta x^3}{\nu^2} = \text{const.} \quad \text{Eq. 62}$$

Similar to Section 2.1, we set the molecular density of both virtual fluids in bulk phases  $n_0^{1*}$  and  $n_0^{2*}$  to be the same, and the bulk phase mass density remains constant in both models. Therefore, the molecular mass of virtual fluid II is given by

$$m^{2*} = 1.3951 m^{1*} = 1.3951 m^1. \quad \text{Eq. 63}$$

Following published work (Kang, Q. *et al.*, 2005) (Schaap, G. *et al.*, 2007), the same-phase fluid interaction strength is set as  $g_{11}^* = g_{22}^* = 0$ . Through detailed analysis, Schaap concluded that the interval for interphase fluid interaction strength  $g_{12}^*$  is  $[0.056, 0.12] G_c$  and he used  $g_{12}^* = 0.1044 G_c$  in his work. Here  $G_c$  is the characteristic interaction strength. This value coincided with  $g_{12}^* = 0.1 G_c$  used in Kang's work (Kang, Q. *et al.*, 2005). However, we found out that using  $g_{12}^* = 0.1 G_c$  will lead to numerical problem at the boundary of the solid phase. We reduced the value of  $g_{12}^*$  to  $0.8 G_c$  as a tradeoff. This guarantees that the pressure of the virtual fluids increase with molecular density. Now the equation of state of the virtual fluids is simply

$$p^* = n^* RT. \quad \text{Eq. 64}$$

According to Schaap's simulation (Schaap, G. *et al.*, 2007), which is consistent with Kang's result (Kang, Q. *et al.*, 2002), and the interfacial tension corresponding to  $g_{12}^* = 0.08 G_c$  is

$$\sigma = 0.04365 p_c \Delta x, \quad \text{Eq. 65}$$

where  $p_c = 3n_0^* RT$  is the characteristic pressure. Substituting the value of  $\Delta x$  and  $p_c$  into Eq. 65, the interfacial tension is given as  $\sigma^* = 78.0413 \text{ N/m}$ . For convenience, we assign the relaxation time of VF I as  $\tau^{1*} = 0.6331 \Delta t$ . In order to keep the viscosity ratio constant,

the relaxation time of VF II is given as  $\Delta x, \Delta t \tau^{2*} = 1.5490 \Delta t$ . To ensure that  $\Pi = \frac{\mu u}{\sigma} = \text{const.}$ , we must have

$$\frac{u^*}{u} = \frac{\sigma^* v}{\sigma v^*} = 0.8625. \quad \text{Eq. 66}$$

Extrapolating the experimental results (Chiquet, P. *et al.*, 2007), the contact angle  $\theta$  of CO<sub>2</sub>-water on quartz is estimated to be 66.4° with brine as the wetting phase (Chiquet, P. *et al.*, 2007). Since sandstone is composed of quartz grains, we choose this value as the contact angle on sandstone. Similar to Section 2.1, we assume that  $g_{1w} = -g_{2w}$ . The interaction strength must satisfy the Yong-Laplace equation (Porter, M. *et al.*, 2009):

$$\cos \theta = \frac{g_{2w} - g_{1w}}{g_{12}}. \quad \text{Eq. 67}$$

Therefore, we fix  $g_{1w} = -g_{2w} = 0.016$ .

The molecular density is expressed as  $n = \Delta n + n_0$ , where  $\Delta n$  is small perturbation and  $n_0$  is the density at injection state. For incompressible flow with a tiny perturbation, we can use the approximation

$$\Delta p = \gamma \Delta n, \quad \text{Eq. 68}$$

where  $\gamma$  is the slope of pressure-density curve at the injection state. From Figure 3, we can obtain the slope of the CO<sub>2</sub> and water curves respectively as  $\lambda^1 = 1550.4 \text{ Pa} \cdot \text{m}^3/\text{mol}$  and  $\lambda^2 = 42857 \text{ Pa} \cdot \text{m}^3/\text{mol}$ . From Eq. 61 and Eq. 64, we have

$$\frac{\Delta n^{1*}}{\Delta n^1} = \frac{\lambda^1 \sigma^*}{RT \sigma} = 1653.2, \quad \text{Eq. 69}$$

$$\frac{\Delta n^{2*}}{\Delta n^2} = \frac{\lambda^2 \sigma^*}{RT \sigma} = 45698. \quad \text{Eq. 70}$$

In the case of gravity driven flow, we have

$$\frac{g^*}{g} = \left( \frac{v^*}{v} \right)^2 = 1.0442 \times 10^7. \quad \text{Eq. 71}$$

Now we can express the whole model with dimensionless numbers marked by subscript d. The variables are normalized as follows:

$$n_d = \frac{n}{n_0}, \quad \text{Eq. 72}$$

$$u_d = \frac{u\Delta t}{\Delta x}, \quad \text{Eq. 73}$$

$$g_d = \frac{g}{G_c}, \quad \text{Eq. 74}$$

$$m_d = \frac{m}{m^1}, \quad \text{Eq. 75}$$

$$\tau_d = \frac{\tau}{\Delta t}. \quad \text{Eq. 76}$$

### 2.3.3. Steady State Distribution in Porous Media

Here, we simulate the process of phase separation and the steady state  $\text{CO}_2$  distribution in the presence of water in a porous medium. In order to meet this objective and simplify the simulation setting, we modified the sandstone model by generating a mirror image of the original pore structure and combined them along the  $x$ – direction as shown in Figure 11. Instead of a pressure BC, periodic BCs are applied at the inlet and outlet. Initially, all of the pore space is randomly assigned with VF I and VF II, then we run the simulation until steady state is reached. Two scenarios are simulated with different  $\text{CO}_2$  saturation  $S_{\text{CO}_2}$ . Figure 12 shows snapshots of phase distributions at different times. It is clear that although the initial distribution is random, driven by different wettability and interfacial tension, droplets of  $\text{CO}_2$  tend to merge together to form larger droplets with smoother surfaces over time. This agrees with the qualitative description of multiphase flow theory.

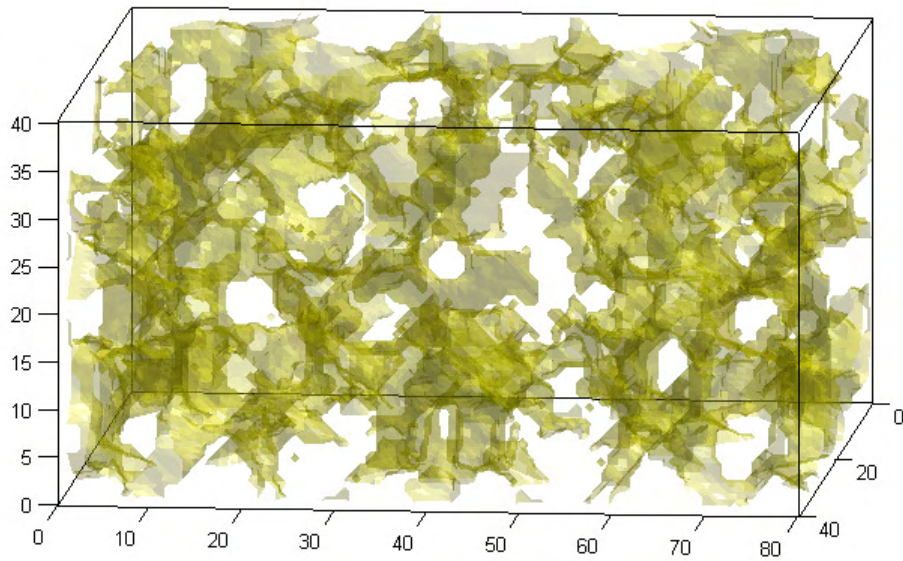
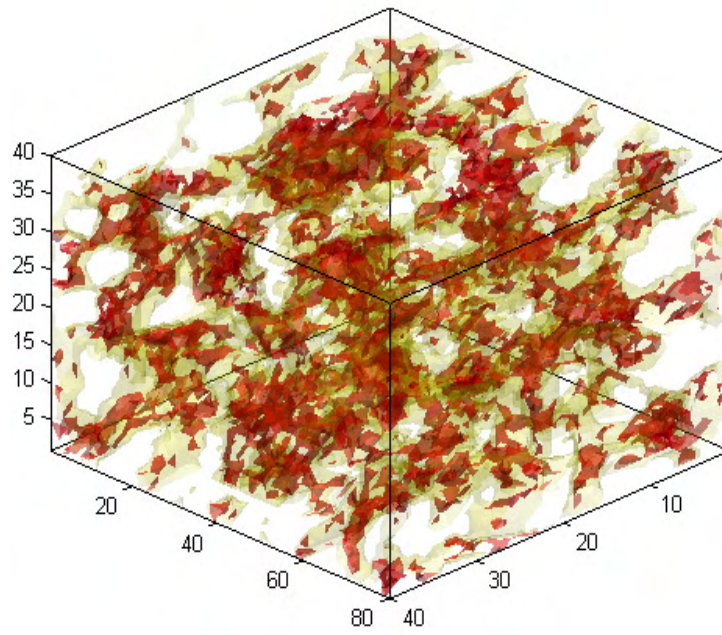
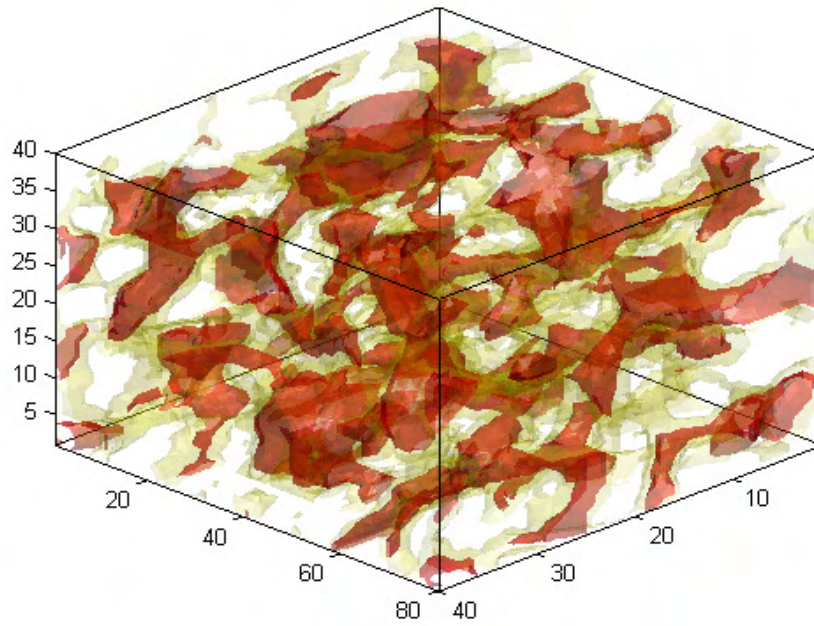


**Figure 11 Modified Pore Structure of Sandstone: Yellow for Void and White for Rock**

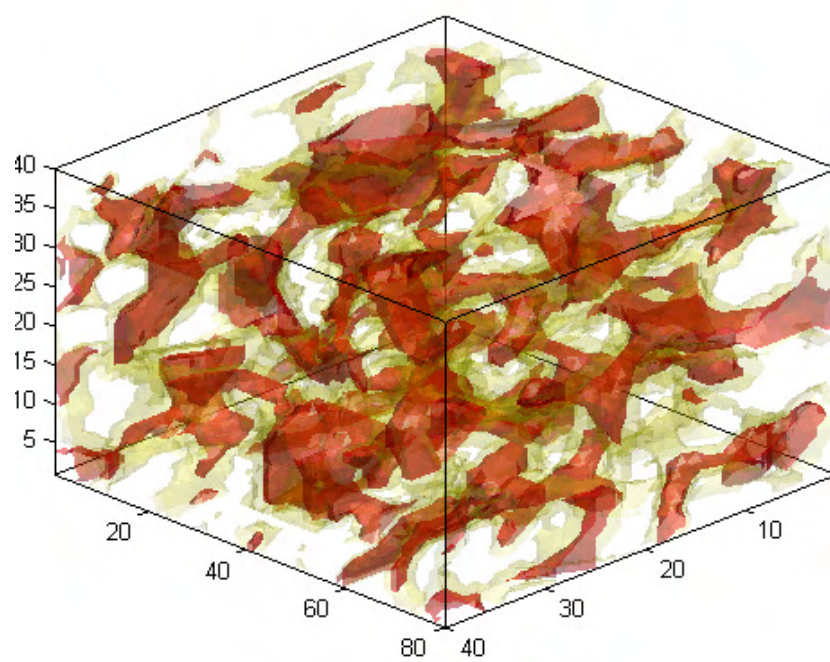


(a)

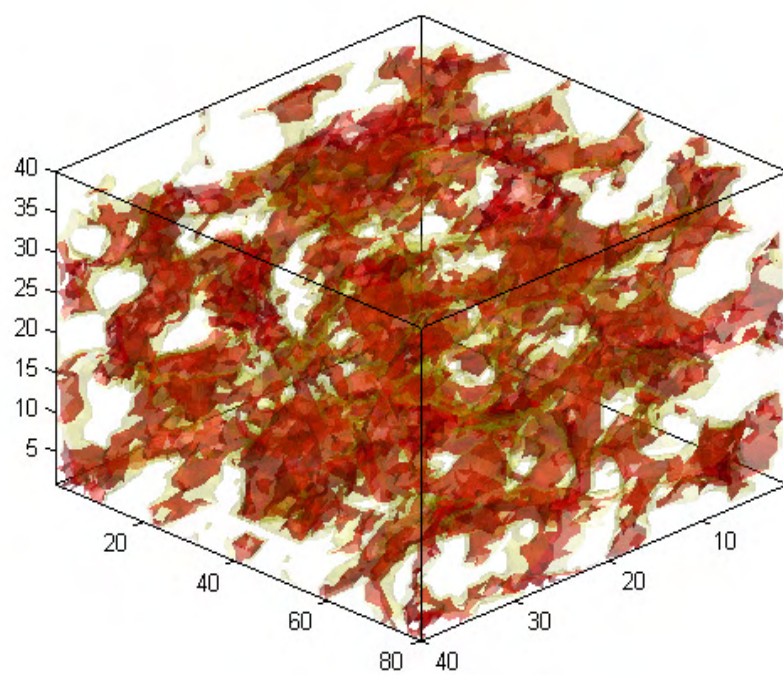


(b)



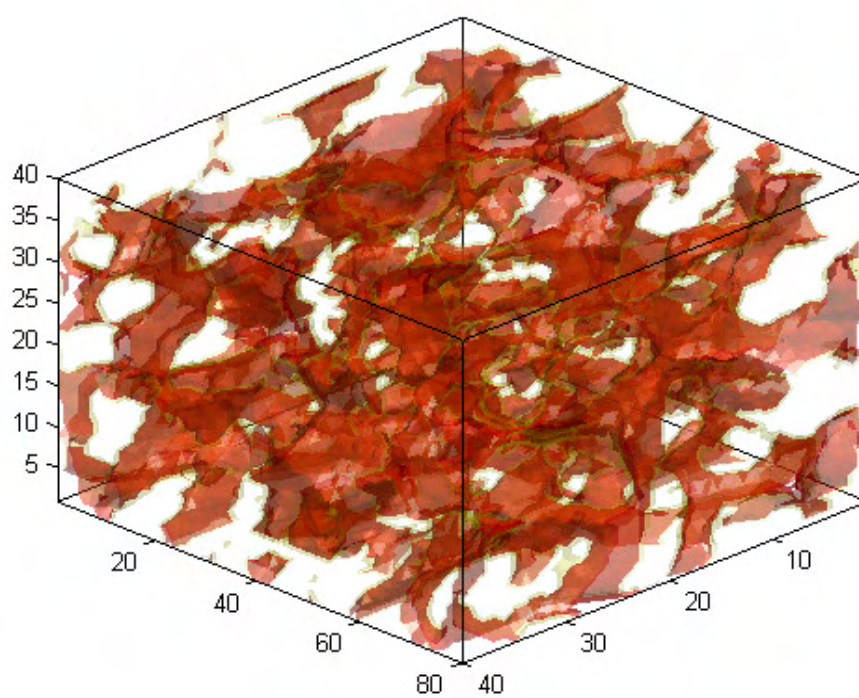


(c)

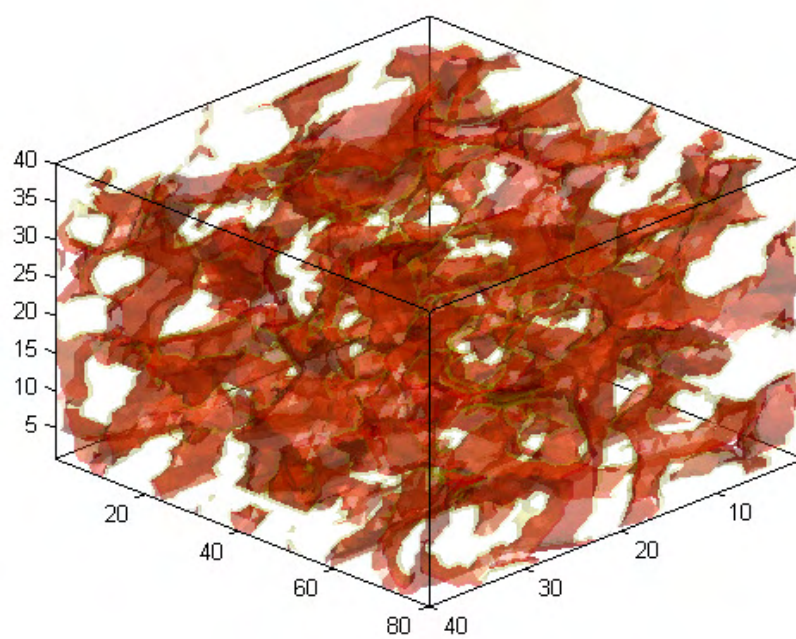


(d)





(e)



(f)

**Figure 12 Phase Distribution in Pore Space: Red for CO<sub>2</sub>, Yellow for Water and White for Rock: (a)-(c)  $S_{CO_2}=0.42$ ,  $t=0, 500$  and  $1000 \Delta t$ ; (a)-(c)  $S_{CO_2}=0.6221$ ,  $t=0, 500$  and  $1000 \Delta t$**

#### 2.3.4. Drainage and Imbibition

In order to study CO<sub>2</sub> flow in sandstone, the pressure boundary condition is applied to the inlet and outlet surfaces. Since in our pressure boundary condition, the macroscopic velocity component  $u_y$  and  $u_z$  are restricted to zero, we add two buffer layers between the pressure boundary and the sandstone. Periodic boundary conditions are applied to the other surfaces. At the beginning, both the inlet and outlet are maintained at the same pressure  $p_0$ . Then we increase the pressure at the inlet as:

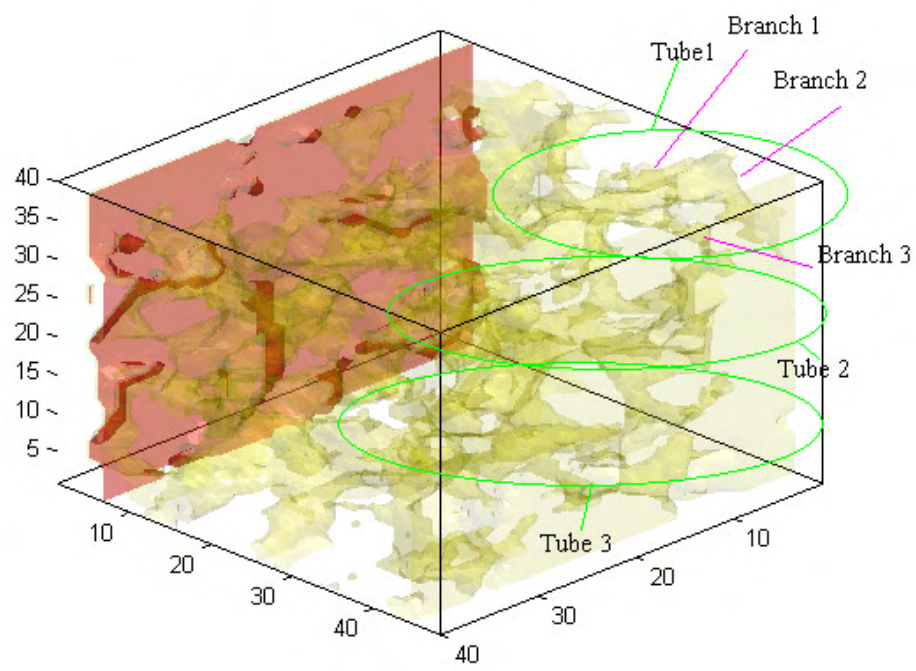
$$p_{in} = \begin{cases} p_0 + \Delta p \frac{t}{T_r}, & t < T_r \\ p_0 + \Delta p, & t \geq T_r \end{cases} \quad \text{Eq. 77}$$

$$p_{out} = \begin{cases} p_0 - \Delta p \frac{t}{T_r}, & t < T_r \\ p_0 - \Delta p, & t \geq T_r \end{cases} \quad \text{Eq. 78,}$$

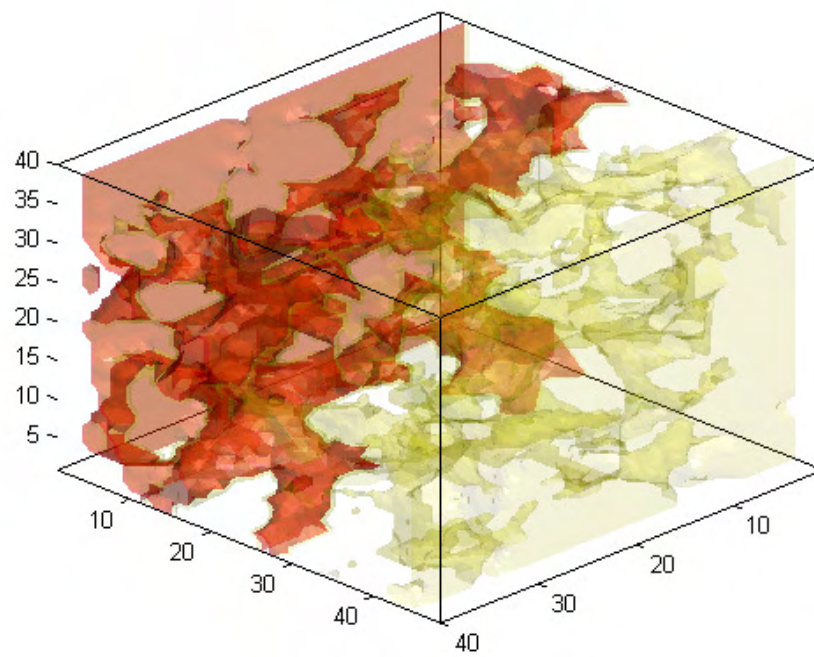
where  $T_r$  is the relaxation time,  $t$  is the number of the current time step and  $\Delta p$  is the constant pressure difference. The pressure at the outlet is always kept at  $p_0$ . We applied constant pressure BC at the inlet and outlet. The pressure difference is fixed at  $\Delta p = 0.2 p_0$ . Since the sandstone is water-wetting, this is a drainage process Figure 13 shows snapshots of the CO<sub>2</sub> plume flow in the drainage process. From the first two snapshots, it is obvious that the CO<sub>2</sub> moves quickly at the beginning. Before  $t = 4000 \Delta t$ , the CO<sub>2</sub> plume has invaded the pore space with the larger average radius compared with other parts of the sandstone. The displacement of water by CO<sub>2</sub> is nearly complete, with almost all the water previously residing in the pore space drained. After that, the propagation of the phase interface is generally slow. In order to better describe the process, we will focus on three tubes formed in the sandstone, of which Tube 1 is further divided into three branches, as depicted in the first snapshot. The CO<sub>2</sub> plume does not penetrate the tubes in Snapshot 2, Tubes 1 and 3 are penetrated in Snapshot 3. As seen in the other tubes, the tip of the CO<sub>2</sub> finger in Tube 3 from Snapshot 3 is very sharp and pointed, which resembles the long finger observed in Hele-Shaw flow with high viscosity ratio. Similar fingers can also be found in Branch 2 of Tube 1 from Snapshot 7 to Snapshot 8. Comparing the CO<sub>2</sub> from Snapshot 8 to Snapshot 11, it can be seen that after the finger reaches a certain length, the propagation of the finger will be mostly radial rather than axial. Also, the CO<sub>2</sub> finger penetrates the pore space with larger average radius, as seen in Branch 1 and 2 from Snapshot 5 to Snapshot 7. Tube 2 is not penetrated until Snapshot 4, since it is connected to the inlet with a narrow throat. Some throats are never penetrated during the simulation, as the one connecting Branch 3 of Tube 1 to Tube 2, since the capillary pressure required exceeds the pressure difference between the

inlet and the outlet. The drainage process is considered completed when the CO<sub>2</sub> distribution reaches steady state. The saturation of CO<sub>2</sub> at the end of the drainage is 73.82%.

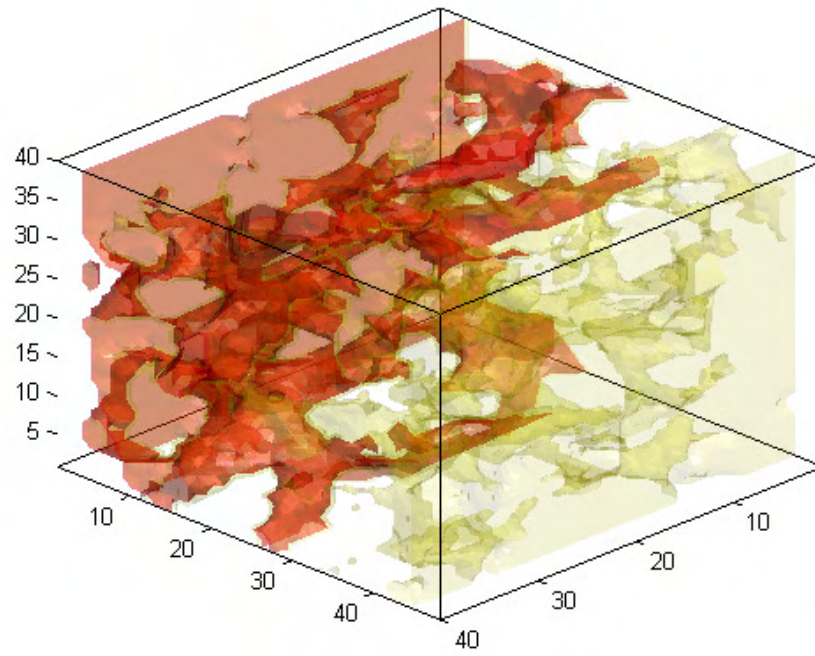
After the drainage process is complete, we simulate water imbibition by reversing the pressure difference to be  $\Delta p = -0.1 p_0$ . The imbibition process is considered completed when the CO<sub>2</sub> distribution reaches steady state. Figure 14 shows snapshots of the CO<sub>2</sub> plume at the end of the imbibition process. The residual saturation of CO<sub>2</sub> at the end of imbibition is 51.77%. Comparing the residual distribution of CO<sub>2</sub> with that right after the drainage process, we can see that the CO<sub>2</sub> plume has retreated from smaller pores, leaving a few disconnected droplets of CO<sub>2</sub> trapped in them.



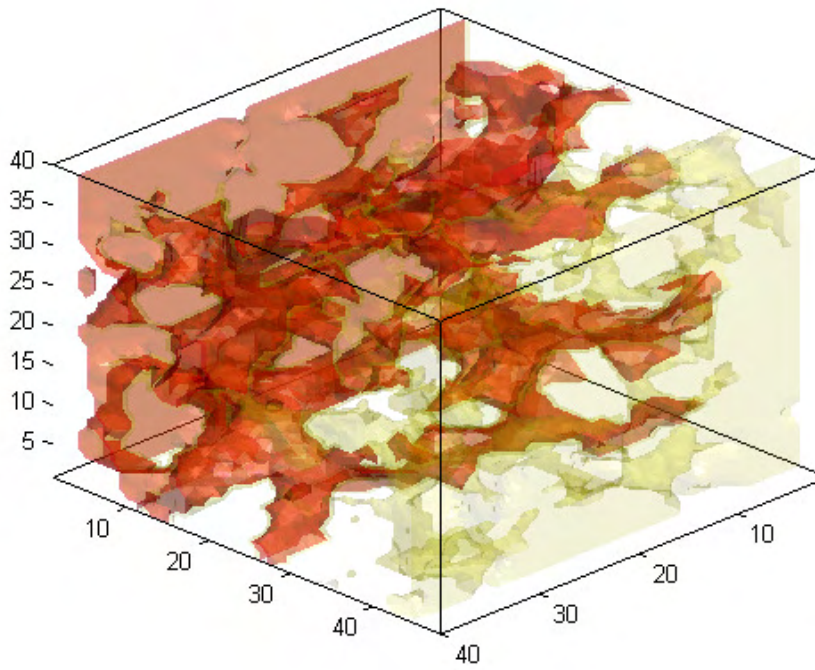
Snapshot 1



Snapshot 2

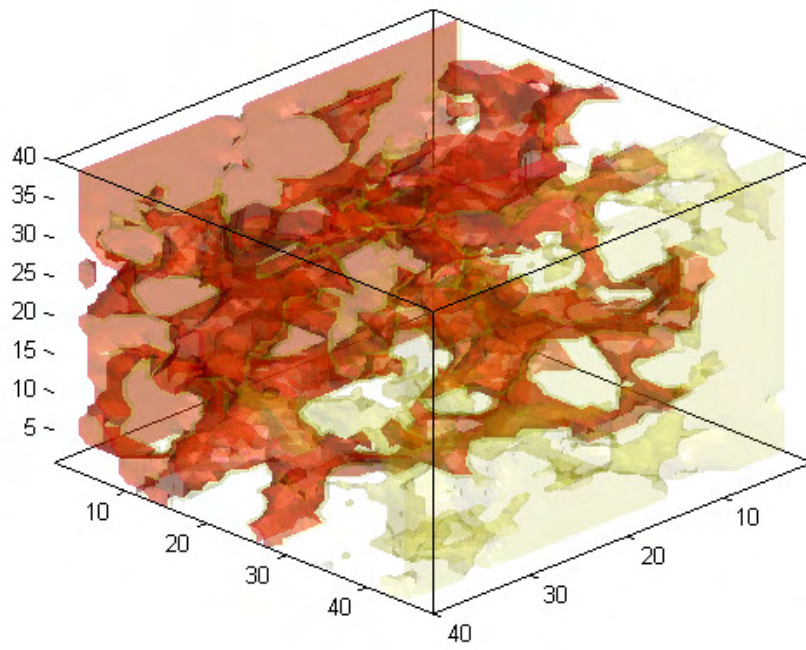


Snapshot 3

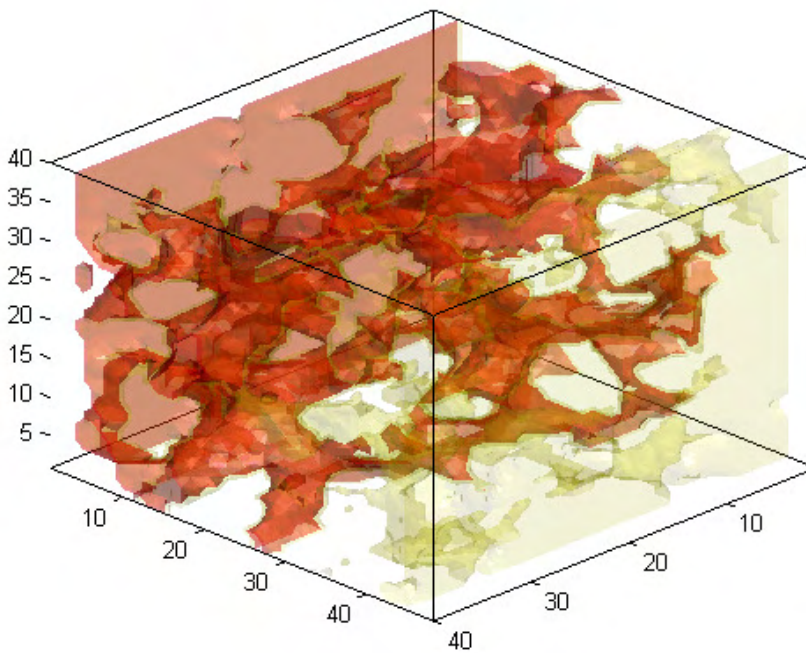


Snapshot 4

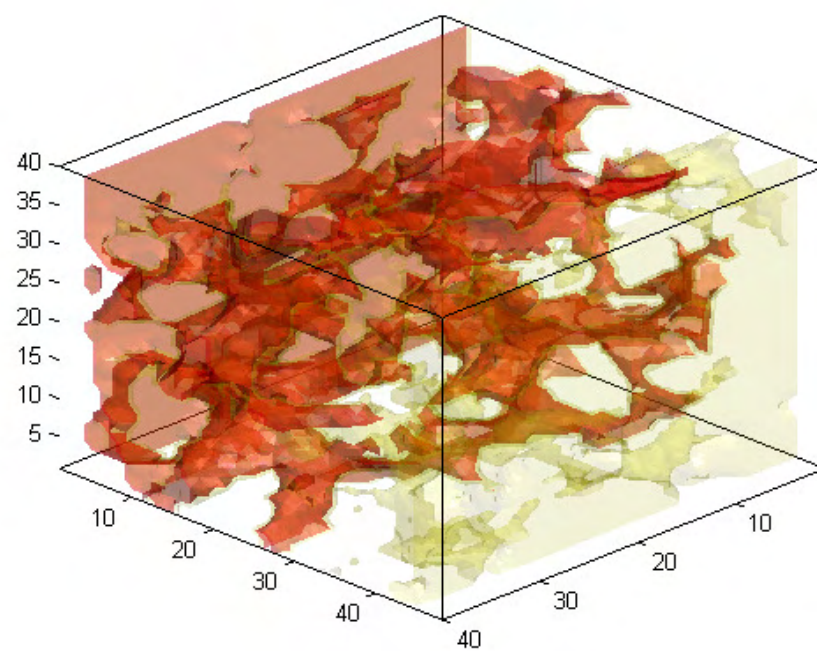




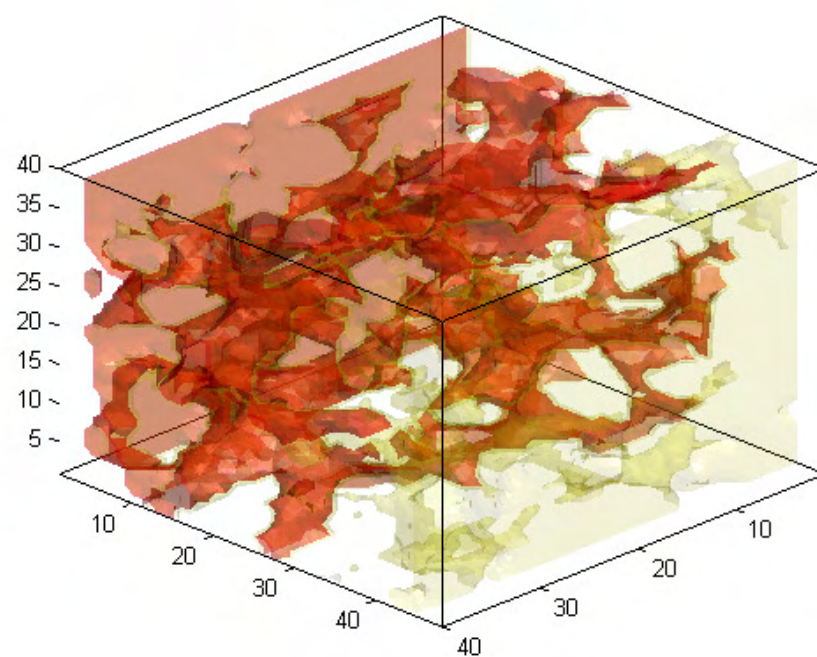
Snapshot 5



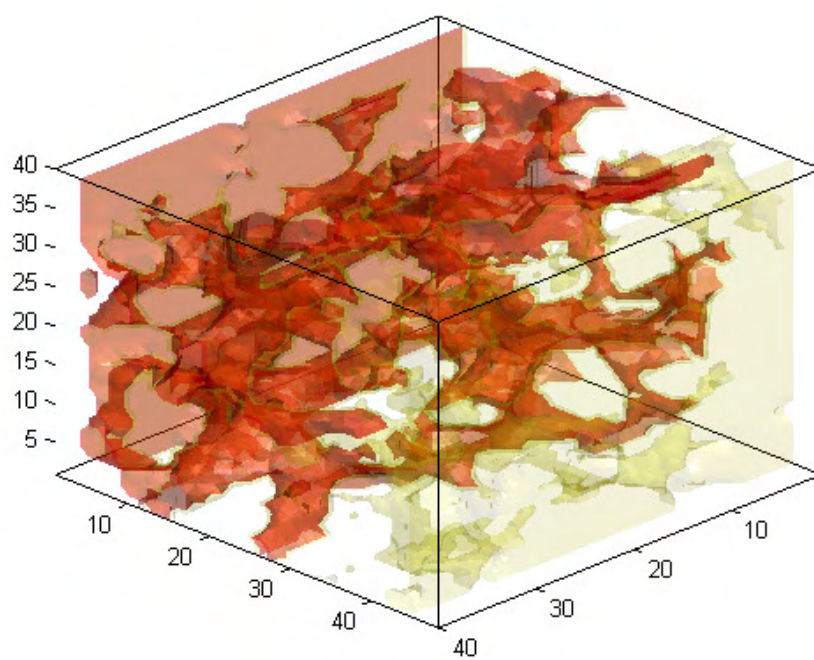
Snapshot 6



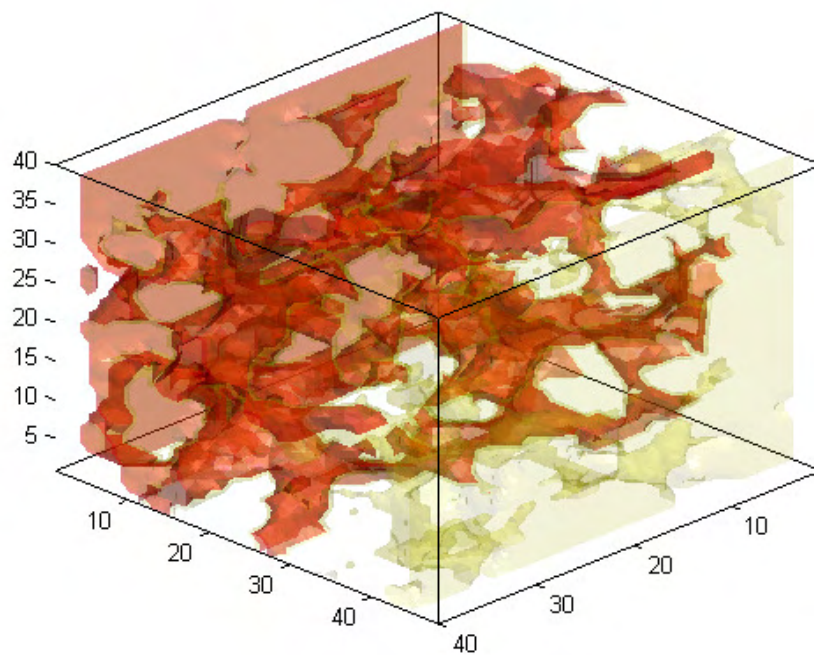
Snapshot 7



Snapshot 8

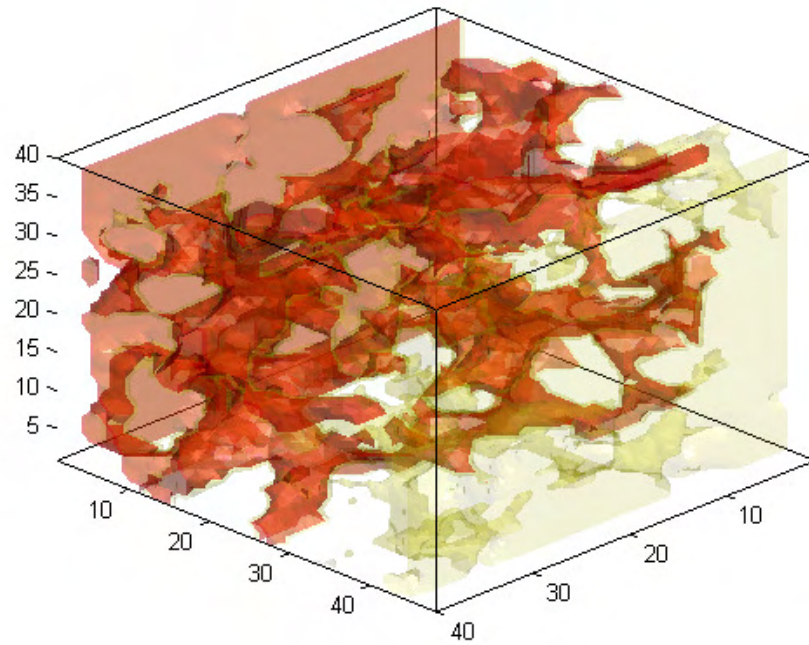


Snapshot 9



Snapshot 10





Snapshot 11

**Figure 13 Snapshots of CO<sub>2</sub> Plume in Fontainebleau Sandstone during Water Drainage, from  $t = 0$  to  $t = 20000\Delta t$  with interval of  $5000\Delta t$  : Red for CO<sub>2</sub>, Yellow for Water and White for Sandstone Grains**

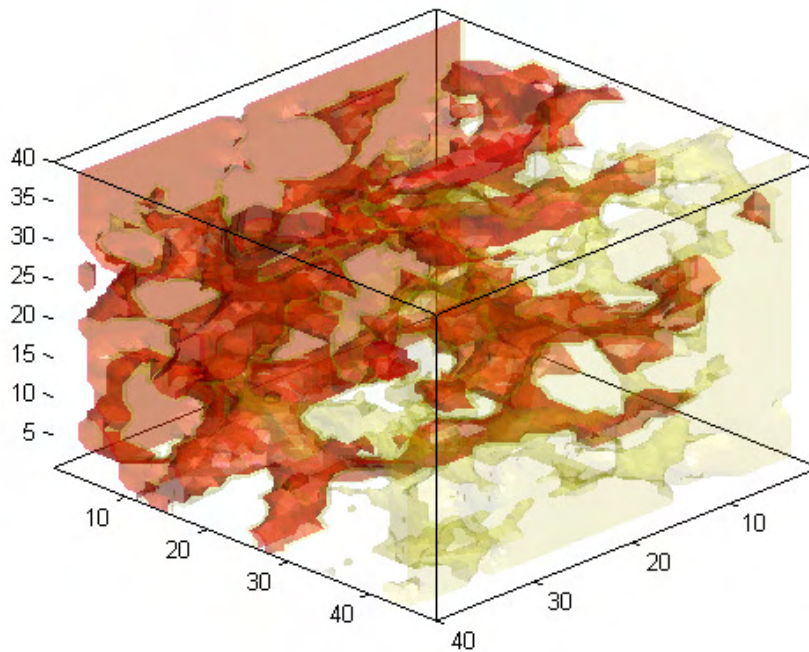


**Figure 14 Snapshots of CO<sub>2</sub> Plume in Fontainebleau Sandstone at the End of Water Imbibition**

## Chapter 3

### 3. Conclusions

In this work, we have reviewed the basic theory of LBM and several multiphase numerical methods based on LBM. Later, we applied the Shan-Chen model to numerical flow simulation. Simulation results are compared with available experimental or theoretical results.

Compared with other multiphase LBM schemes, the Shan-Chen model is relatively easy to implement and able to capture the fundamental hydrodynamic features such as interfacial tension and wettability. Therefore, the Shan-Chen model was used. To validate the method, we simulated steady-state single flow in a pack of beads. The simulations agree well with the experimental results. Also, we simulated viscous fingering in long 2D tubes. The simulations agree well with the theoretical predictions. However, the Shan-Chen model has difficulties in modeling immiscible multiphase flow in porous media for real fluids. To overcome the difficulties, we introduced a similitude model. We simulated multiphase flow in porous media using parameters that have been proved feasible for the Shan-Chen model and derived relationships between hydrodynamic variables in the similitude model and the real model.



## References

- Bhatnagar, P. *et al.*, 1954, “A Model for Collision Process in Gases. I. Small Amplitude Processes in Charged and Neutral One-Component Systems”, *Physical Review*, 94, 511-525
- Chalbaud, C. *et al.*, 2009, “Interfacial Tension Measurements and Wettability Evaluation for Geological CO<sub>2</sub> Storage”, *Advances in Water Resources*, 32, 98-109
- Chang, C. *et al.*, 2009, “Boundary Conditions for Lattice Boltzmann Simulations with Complex Geometry Flows”, 58, 940-949
- Chen, H. *et al.*, 1992, “Recovery of the Navier-Stokes Equations Using a Lattice-gas Boltzmann Method”, *Physical Review A*, 45, 5339-5342
- Chen, S. and Doolen G., 1998, “Lattice Boltzmann Method for Fluid Flows”, *Annual Review of Fluid Mechanics*, 30, 329-364
- Chen, S. *et al.*, 1992, “Lattice Boltzmann Computational Fluid Dynamics in Three Dimensions”, *Journal of Statistical Physics*, 68, 379-400
- Chiquet, P. *et al.*, 2007, “Wettability Alteration of Caprock Minerals by Carbon Dioxide”, *Geofluids*, 7, 112-122
- Cornubert, R. *et al.*, 1991, “A Knudsen Layer Theory for Lattice Gases”, *Physica D*, 47, 241-259
- d'Humières, D., 1992, “Generalized Lattice Boltzmann Equations”, *Rarefied Gas Dynamics: Theory and Simulations, Progress in Aeronautics and Astronautics*, 159, 450-458
- d'Humières, D., 2002, “Multiple-relaxation-time Lattice Boltzmann Models in Three Dimensions”, *Philosophical Transactions of the Royal Society A*, 360, 437-451
- Frisch, U. *et al.*, 1986, “Lattice-Gas Automata for the Navier-Stokes Equation”, *Physical Review Letters*, 56, 1505-1508
- Frisch, U. *et al.*, 1987, “Lattice Gas Hydrodynamics in Two and Three Dimensions”, *Complex System*, 1, 649-707
- Finney, J., 1970, “Random packings and structure of simple liquid: I. The geometry of random close packing”, *Proceedings of the Royal Society A*, 319, 479-493
- Gunstensen, A. *et al.*, 1991, “Lattice Boltzmann Model of Immiscible Fluids”, *Physical Review A*, 43, 4320-4327

- Gropp, W. *et al.*, 1994, “Using MPI: portable parallel programming with the message-passing interface”. 1<sup>st</sup> Ed., MIT Press Scientific And Engineering Computation Series, Chapter 3
- Grunau, D. *et al.*, 1993, “A Lattice Boltzmann Model for Multiphase Fluid Flows”, *Physics of Fluids A*, 5, 2557-2562
- Halpern, D. and Gaver, D., 1994, “Boundary Element Analysis of the Time-Dependent Motion of a Semi-infinite Bubble in a Channel”, *Journal of Computational Physics*, 115, 366-375
- He, X *et al.*, 1999, “A Lattice Boltzmann Scheme for Incompressible Multiphase Flow and Its Application in Simulation of Rayleigh-Taylor Instability”, 152, 642-663
- He, X. and Doolen, G., 2002, “Thermodynamic Foundations of Kinetic Theory and Lattice Boltzmann Models for Multiphase Flows”, *Journal of Statistical Physics*, 107, 309-328
- Hou *et al.*, 1997, “Evaluation of Two Lattice Boltzmann Models, for Multiphase Flows”, *Journal of Computational Physics*, 138, 695-713
- Kang, Q. *et al.*, 2002, “Displacement of a Two-dimensional Immiscible Droplet in a Channel”, *Physics of Fluids*, 14, 3203-3214
- Kang, Q. *et al.*, 2004, “Immiscible Displacement in a Channel: Simulations of Fingering in Two Dimensions”, *Advances in Water Resources*, 27, 13-22
- Kang, Q. *et al.*, 2005, “Displacement of a Three-dimensional Immiscible Droplet in a Duct”, *Journal of Fluid Mechanics*, 545, 41-66
- Kline, S., 1965, “Similitude and Approximation Theory”, 1<sup>st</sup> Ed., McGraw-Hill, Chapter 2
- Krzikalla, F. *et al.*, 2010, “Understanding the Effects of Salt Precipitation on Rock Microstructure by Using Digital Rock Technology”, AGU Fall Meeting, MR51A-1889
- Lallemand, P. and Luo, L., 2000, “Theory of the Lattice Boltzmann Method: Dispersion, Dissipation, Isotropy, Galilean Invariance, and Stability”, *Physical Review E*, 61, 6546-6562
- NIST Chemistry WebBook, <http://webbook.nist.gov/chemistry/fluid/>
- Niu, X. *et al.*, 2007, “An Investigation of Water-Gas Transport Processes in the Gas-diffusion-layer of a PEM Fuel Cell by a Multirelaxation-time Lattice Boltzmann Model”, *Journal of Power Sources*, 172, 542-552

- Porter, M. *et al.*, 2009, “Lattice-Boltzmann Simulations of the Capillary Pressure-Saturation-Interfacial Area Relationship for Porous Media”, *Advances in Water Resources*, 32, 1632-1640
- Qian, Y. *et al.*, 1992, “Lattice BGK Models for Navier-Stokes Equation”, *Europhysics Letters*, 17, 479-484
- Reid, R. *et al.*, 1987, “The Properties of Gases and Liquids”, McGraw-Hill, 4<sup>th</sup> Ed., Chapter 11
- Sbragaglia, M. *et al.*, 2007, “Generalized Lattice Boltzmann Method with Multirange Pseudopotential”, *Physical Review E*, 75, 026702
- Schaap, G. *et al.*, 2007, “Comparison of Pressure-Saturation Characteristics Derived from Computed Tomography and Lattice Boltzmann Simulations”, *Water Resources Research*, 43, W12S06
- Shan, X. and Chen, H., 1993, “Lattice Boltzmann Model for Simulating Flows with Multiple Phases and Components”, *Physical Review E*, 47, 1815-1820
- Shan, X. and Doolen, G., 1995, “Multicomponent Lattice-Boltzmann Model with Interparticle Interaction”, *Journal of Statistical Physics*, 81, 379-383
- Shan, X. and Doolen, G., 1996, “Diffusion in a Multicomponent Lattice Boltzmann Equation Model”, *Physical Review E*, 54, 3614-3620
- Swift, M. *et al.*, 1995, “Lattice Boltzmann Simulation of Nonideal Fluids”, *Physical Review Letters*, 75, 830-834
- Swift, M. *et al.*, 1995, “Lattice Boltzmann Simulations of Liquid-Gas and Binary Fluid Systems”, *Physical Review E*, 54, 5041-5052
- White, J., *et al.*, 2006, “Calculating the Effective Permeability of Sandstone with Multiscale Lattice Boltzmann/Finite Element Simulations”, *Acta Geotechnica*, 1, 196-209
- Yuan, P. and Schaefer, L., 2006, “Equations of State in a Lattice Boltzmann Model”, *Physics of Fluids*, 18, 042101
- Zheng, H. *et al.*, 2006, “A Lattice Boltzmann Model for Multiphase Flows with Large Density Ratio”, *Journal of Computational Physics*, 218, 353-371